ChemComm

ROYAL SOCIETY OF CHEMISTRY

REVIEW ARTICLE

View Article Online
View Journal

Cite this: DOI: 10.1039/d5cc06934c

Nonspherical polymer nano/micro particles: a guide to shape engineering

Jeremiah James,[ab] Emma Leung[b] and Rong Yang *[a]

Polymer micro- and nanoparticles underpin applications from drug delivery to building materials, yet virtually all commercial grades of polymer particles are spherical, forfeiting the performance gains unlocked by shape engineering. In drug delivery, for instance, shape-engineered polymer particles promise longer circulation, targeted tissue penetration, programmable assembly, and tailored photonic responses, positioning geometry as an under-exploited design axis. Although three decades of lab-scale research have produced dozens of protocols for producing shaped polymer particles, a mechanism-centric roadmap that links fabrication route to attainable morphology has been missing. This review closes that gap by surveying more than 70 documented geometries and the physicochemical principles that create them. In brief, starting from the spherical polymer particles, mechanical deformation, such as film stretching, compression, and shear, reshapes spheres into rods, ellipsoids, discs, and polyhedra using low-cost tensile/compressive bench-top rigs. Increased complexity in particle shapes can be obtained *via* lithographic and template-molding platforms, yielding cuboids, prisms, rings, and sub-100 nm flakes with dimensional fidelity. By expanding upon the polymerization mechanism beyond photopolymerization, seeded emulsion polymerization exploits polymerization-induced phase separation to generate lobed, Janus, porous, and indented architectures while retaining a reasonable production throughput. Polymerization under shear, such as masked photopolymerization under continuous microfluidic confinement, cast plugs, prisms, high-curvature ''hamburger'' or ''olive'' motifs, and other extruded forms. Emerging template-free and confinement-free techniques, such as polymer plasticization, condensed-droplet polymerization, and electrospraying, expand the landscape to asymmetric shapes, leveraging interfacial tensions, condensation kinetics, and electric fields to sculpt morphology. Looking ahead, green chemistries and scalable process design constitutes critical steps that will unlock the societal impact of this emerging class of materials. This review aims to organize those disparate methods based on their fundamental mechanisms, thereby accelerating the design, synthesis, and production of shape-engineered soft materials, pointing to novel solutions in healthcare, consumer goods, structural materials, and active matter and robotics.

Received 4th December 2025,
Accepted 5th March 2026

DOI: 10.1039/d5cc06934c

rsc.li/chemcomm

1. Introduction

Virtually all commercially available polymer micro- and nanoparticles share a single geometry: sphere. This ubiquity is a direct consequence of the synthesis and production technology. The modern polymer particle industry traces its roots to World War II, when the U.S. government launched a synthetic rubber initiative to replace natural rubber imports cut off from Southeast Asia.[1] The effort culminated in the industrial-scale adoption of emulsion polymerization, a process that rests on the fundamental principle of polymerization in monomer-swollen micelles.[2,3] In a typical process, hydrophobic monomers are dispersed within an aqueous medium, using surfactants to form stable micellar droplets, which are then polymerized by radical initiators into solid particles.[4] Because the micelles adopt a spherical shape to minimize their interfacial energy in water, this symmetry is preserved as polymerization locks the morphology in place.[5] The dominance of emulsion polymerization in the particle manufacturing industry thus entrenched the spherical form as the industry standard, inadvertently constraining access to the performance gains that shape engineering could unlock.[6]

The ability to deliberately engineer particle shape expands the design space of polymer-based micro- and nanostructures, unlocking functions inaccessible to conventional spherical

[a] Robert Frederick Smith School of Chemical and Biomolecular Engineering, Cornell University, Ithaca, NY, 14853, USA. E-mail: ryang@cornell.edu
[b] Nancy E. and Peter C. Meinig School of Biomedical Engineering, Cornell University, Ithaca, NY, 14853, USA

particles. The opportunities afforded by shape-engineered polymer particles are most evident in drug delivery, where decades of research have optimized materials and formulations but seldom geometry until recently. Since their emergence in the mid-to-late twentieth century, liposomes and polymer-based delivery vehicles have served as foundations for modern nanomedicine by modulating the bioavailability of therapeutics, delaying their clearance, and reducing off-target toxicity.[7–9] Research over the last decades has further expanded the material palette to metals (for electromagnetic or catalytic properties), dendrimers (to enable large payloads), carbon nanomaterials, and combinations of those constituents that give rise to hybrid materials.[10] Among these, polymer-based delivery vehicles stand apart for their tunability in three critical design axes: chemistry, size, and shape. Through monomer and polymer selection, the chemistry is tuned to regulate release kinetics and responsiveness to biological or environmental stimuli.[11–13] The sizable library of biocompatible polymers, ranging from natural biopolymers and polysaccharides to synthetic biodegradable amides or esters, and non-biodegradable siloxanes or acrylics, has created a rich chemical toolbox.[14] Similarly, size engineering has been extensively optimized to balance circulation time, tissue penetration, and biological interactions for targeted delivery and/or pharmacokinetics.[15–18] Taken together, these advances have propelled polymer particles toward clinical translation: almost 40 nanoparticle formulations have been clinically approved with more on the way, such as docetaxel-loaded polymeric particles (CPC634) that have entered clinical testing.[15] Despite decades of progress in chemistry and size control, nearly all clinically approved nanomedicine to date remains spherical or near-spherical. As such, shape engineering becomes a powerful yet underutilized axis in the design of drug delivery vehicles.[16] Emerging evidence underscores that shape-engineered polymer particles can outperform their spherical counterparts across multiple therapeutic benchmarks. Low-curvature geometries prolong circulation by evading macrophage-mediated clearance pathways, while elongated or

Jeremiah James

Jeremiah James graduated with a PhD in Engineering from Cornell University, where his work lay at the intersection of polymer science, materials engineering, and biomedical engineering. His research focused on condensed droplet polymerization and the design of shape-engineered polymer micro- and nanoparticles, with broader interests in controlled morphology, functional materials, and translatable systems. Through his work, he developed expertise in materials synthesis, particle fabrication, characterization, and particle–property relationships, with an emphasis on connecting fundamental engineering principles to practical challenges in health and technology. His broader interests include innovation at the interface of engineering, applied problem-solving, and scalable systems.

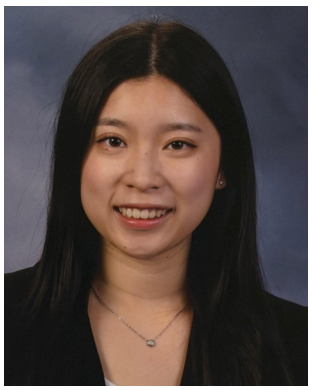

Emma Leung

Emma Leung is an undergraduate student at Cornell University studying biomedical engineering. Her research interests include particle fabrication, characterization, and their applications. She is a recipient of the Cornell Office of Inclusive Excellence Undergraduate Research Award. Following graduation, Emma will be pursuing a career in the medical device industry.

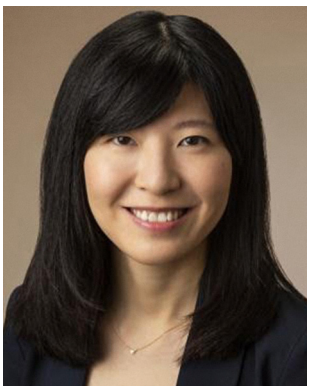

Rong Yang

Dr. Rong Yang is the Marjorie L. Hart Professor of Engineering and an Associate Professor at the Robert F. Smith School of Chemical and Biomolecular Engineering at Cornell University. She received her BS in Chemical Engineering from Tsinghua University in Beijing and her PhD in Chemical Engineering from MIT, working with Karen Gleason. From 2014–2016, she was a postdoctoral fellow at Boston Children's Hospital and Harvard Medical School, working with Daniel Kohane and Robert Langer, where she later became an Assistant Professor before joining Cornell in 2019. Her research lies at the intersection of material science and biomedical engineering, with a focus on all-dry polymer synthesis techniques, functional nano- or living materials with controlled morphology and reactivity, and their application in drug delivery, infectious disease treatment, and environmental sustainability. Her work has been recognized by the NIH Pathway to Independence Award, the NSF CAREER Award, and the Camille Dreyfus Teacher-Scholar Award, among others.

anisotropic particles improve margination, tumor penetration, and endothelial adhesion.[17,18] Such findings reveal geometry as a potentially synergistic design variable alongside chemistry and size, which critically governs the flow, jam, and stimuli-responsive behaviors of polymer particles in biological systems.

Despite the growing recognition of geometry as a design variable, current synthesis strategies for nonspherical polymer particles remain confined largely to the laboratory scale. Few existing techniques have achieved the throughput, reproducibility, or process economy required for industrial adoption. The barriers are rooted in complex multistep procedures, narrow parameter windows, and limited scalability. This review surveys the current landscape of shape-engineering methods, linking attainable morphologies to their governing physicochemical mechanisms. Beyond the emulsion polymerization routes that established the dominance of spherical particles, emerging fabrication strategies have diversified the particle-shape repertoire.[19–21] Lithographic and template-molding platforms offer high precision in the *xy*-plane, producing nano- to micro-scale cuboids, prisms, and rings through patterned photomasks, molds, or interference fields, albeit with throughput constraints inherent to planar processing. Seeded emulsion polymerization exploits polymerization-induced phase separation to access lobed, Janus, hollow, and dimpled architectures within industry-familiar emulsification systems. Mechanical deformation approaches, such as film stretching, compression, or shear, reshape spherical feedstock into rods, ellipsoids, and polyhedra using low-cost tools, though shape uniformity can vary. Microfluidic photopolymerization achieves high-fidelity confinement-defined geometries, generating monodisperse plugs, discs, and prisms, yet remains limited by device throughput. Finally, template-free strategies such as solvent-vapor annealing, vapor-phase polymerization, condensed-droplet polymerization (CDP), and electrospraying leverage interfacial tension, condensation dynamics, and electric fields to create shapes unattainable through conventional routes. Despite the rapid development in the past three decades, the guiding principles that connect the fabrication routes to their resulting geometries remain elusive. This review aims to close that gap by cataloguing over seventy experimentally realized geometries and mapping each to its fundamental mechanism. We hope to empower researchers to quickly gain access to their targeted particle shapes through the detailed description of the mechanism, instrumentation, and processes involved in each methodology that can be found in this review. In doing so, we aim to open up the polymer shape engineering toolbox and accelerate translation of some of the methodologies into industrial practice, driven by future use-inspired developments. To help readers compare the major synthesis methods on equal footing, Table 1 consolidates the key practical considerations for each approach. Specifically, it summarizes (i) the operative mechanism that generates anisotropy, (ii) the polymerization/solidification mode, and (iii) the dominant polymer/material classes reported, alongside size ranges, throughput/scale, biomedical relevance, and method-specific advantages and limitations.

2. Strategies for shape-engineered polymer nano/micro particles

2.1. Lithography

Lithographic platforms create nonspherical polymer particles by spatially patterning crosslinking within photosensitive films, delivering unmatched in-plane fidelity and narrow polydispersity.[22] In conventional mask-based photolithography, a photoresist—typically composed of an oligomer/polymer matrix, a multifunctional acrylate crosslinker, and a radical photoinitiator—is spin-coated onto a substrate and exposed to UV light through a patterned photomask (Fig. 1a). When a positive photoresist is used, the exposed regions polymerize while unexposed areas are removed during development, and vice versa for a negative photoresist. The resulting photomask-defined pattern in the *x*-*y* plane penetrates through the resist thickness, defining the particle height in the *z*-direction.

Using a UV-curable oligomeric solution as the photoresist, cuboid particles with edge lengths between 5 and 200 μm have been fabricated (Fig. 1a).[23] In addition to the common ingredients of a positive photoresist formulation, a volatile solvent such as dimethylformamide (DMF) can be included to improve film uniformity during spin-coating. As such, a representative positive photoresist formulation includes polyvinylpyrrolidone (PVP), trimethylolpropane ethoxylate triacrylate), DMF, and 2,2-dimethoxy-2-phenylacetophenone (DMPA, which can be activated during UV exposure). After spin-coating and solvent evaporation (typically *via* baking), curing is achieved *via* UV exposure through a square-patterned mask, generating radicals that crosslink the illuminated regions. Subsequent rinsing with isopropyl alcohol removes the unexposed material, revealing cuboid microparticles. Immersion in Tris–EDTA containing Tween-20 swells the lightly crosslinked network and reduces the wafer–particle interfacial tension, enabling clean detachment. Repeated spin-coat/bake cycles allow layer-by-layer (LbL) stacking of chemically distinct films—such as poly(ethylene glycol) (PEG200) or poly(allylamine hydrochloride) (PAH)—to build semi-interpenetrating polymer networks that enhance mechanical robustness or encode function. For instance, PEG or PAH layers can introduce porosity or DNA-binding capability, whereas alternating FITC- and TRITC-dextran-doped layers generate fluorescent ''barcodes''.

Beyond mask-based approaches, lithographically fabricated polymer particles can also be produced without masks. Interference lithography (IL) is a maskless technique that uses the interference of coherent laser beams to create periodic, three-dimensional light intensity patterns within a photosensitive medium (Fig. 1b).[24,25] Polymerization occurs only in regions of constructive interference, eliminating the need for costly photomasks and allowing rapid prototyping of complex geometries. After UV exposure, the solidified network forms a lattice of interconnected microstructures, which can be released as individual particles *via* mild dry etching or mechanical agitation. IL has been used to generate cubic, prismatic, and spinning-top particles (Fig. 1b). Although polymerization occurs volumetrically rather than on a planar substrate, the overall throughput

Table 1 Comparative summary of method families for synthesizing non-spherical polymer particles. For each method, the table outlines the anisotropy mechanism and processing mode, the dominant polymer/materials reported, and representative particle-size bins and scale/throughput indicators, together with explicit strengths, limitations, and biomedical relevance

Field	2.1 Lithography	2.2 Seeded emulsion polymerization	2.3 Mechanical deformation	2.4 Microfluidic	2.5 Misc
Summary	Anisotropy is set by a mask/interference pattern or mold cavity UV/thermal curing (or solidification) locks geometry, followed by release/harvest of freestanding particles or structures.[22–39]	Anisotropy emerges during seed swelling and polymerization-induced phase separation/protrusion growth, with morphology controlled by crosslink density, monomer-seed ratio, and kinetics.[40–80]	Pre-formed particles are softened (heat above T_g or use solvent/plasticizer) and mechanically deformed (stretching, hot-press, squeeze flow) to lock anisotropy the deformation step itself does not require polymerization.[81–96]	Droplet or laminar-flow templates formed in microchannels are solidified (typically by UV FRP) confinement, flow, and multiphase droplet physics set nonsphericity and compartmentalization.[97–116]	Anisotropy arises without lithographic molds: interface-/film-based reshaping by thermal/solvent/vapor annealing vapor CDP (condense monomer droplets → FRP) electrospray droplet drying/collapse ionotropic gelation and biomimetic templating.[117–132]
Polymerization	Often UV-initiated free-radical photopolymerization/photocrosslinking (hydrogels, photoresists, acrylates), with some thermal FRP (*e.g.*, triacrylate arrays) in micromolding of pre-formed polymers, the shaping step itself does not require polymerization.[22–39]	Predominantly FRP (persulfate/azo/thermal or radiation-initiated) in seeded emulsion/dispersion workflows some systems add post-polymerization chemistry (*e.g.*, sacrificial phases).[40–80]	Deformation step does not require polymerization precursor particles are commonly made by emulsion solvent evaporation (*e.g.*, PLGA/PCL) or by polymerization when using PS/PMMA/PDVB model systems.[81–96]	Predominantly UV-initiated FRP of acrylate/methacrylate monomers in droplets or laminar streams some platforms include sol–gel/surface chemistry steps for wettability patterning.[97–116]	Mixed: reshaping/annealing steps have no polymerization CDP uses TBPO-initiated FRP electrospray uses pre-formed polymers alginate uses ionic crosslinking (Ca^{2+}) RBC-mimic shells are crosslinked chemically (*e.g.*, glutaraldehyde).[117–132]
Polymers	PEG-based hydrogels[23,26,30,38] Epoxy photoresists[24,25,32] Thermoplastics and biodegradable polyesters[31,34] Acrylate-based[39]	PS systems[43–52,61–65,72–77] PMMA-based[44,49,54,57,78] Methacrylate/epoxy systems[48,58,59,75] Bio-derived composites[42] TPM-based[70,71] TPM-based[70,71] Polymer-inorganics[47,66,68,69]	PLGA[81,82,85,86,94] PS[84,89,91,93,94,96] PLA[87,94] PDVB[95] PIBCA[92] Polymer blends[90]	Polyacrylate.[97,100,103–105,109,112,115,116] PEGDA.[110,111,113–116] PETPTA.[107]	PS[117–123] Methacrylates[124–127] PLGA[129,130] Alginate.[131] Protein/polyelectrolyte.[132]
Sizes	0–1 μm[24–26,28,30,32,38] 1–10 μm.[22,23,31,34–37] >10 μm.[22,23,29,30,34–37,39]	0–1 μm[41,42,46–52,55–57,59,64–66,68,69,71–76,79,80] 1–10 μm[41,43–46,48,50–55,58–63,65,69–73,76–80] >10 μm[43,46,48,55,56,59]	0–1 μm[81,83–86,89–94,96] 1–10 μm[81–85,87–91,93,94] >10 μm[82,89,94,95]	0–1 μm (not reported) 1–10 μm[97,103,116] >10 μm.[97,100–115]	0–1 μm[122,124,125] 1–10 μm[117,119–123,129,130] >10 μm.[119,120,126,127,131]
Shapes	Mask-/mold-defined planar and extruded geometries (*e.g.*, polygons, rods, boomerrang)[22,23,29,30,32,37,38] Cone[31] Flakes[39]	Polygons/polyhedra[40,42,61,63,65] Rods[40,61] Disks/discoids[47,63,73] Ellipsoids/spheroids[45,48,69] Locks/keys[70,71] Lobed/clusters[40,42–51,54,57,61–63,68,70] Capsules/shells[41,66,68,78] Janus[46–48,57–59,64,68,72,76]	Polygons/polyhedra[89,96] Rods/cylinders[82,86,89,93] Disks[81,85,89–94] Ellipsoids[81–84,86–93] Lobed/clusters[84] Concave/dimpled/bowls[84,89,90] Capsules/shells[95] Lens-like[89] Jellyfish-like[81,89]	Disks/rods/ellipsoids[97,100] Janus/shells/crescents[101,102,104,108,109,112] Mask-defined extruded 2D shapes[106,110,112–116]	Lenses/acorns/discs/bowls/peanuts and other concave morphologies[117–123] Domes/plates[124–127] Rods[129,130] Tadpole/tear shapes[131] RBC-mimic[132]
Limitations	Release-layer challenges/particle loss[22] Supercritical CO_2 drying[25] Flakes can stick/break on PDMS release[39] PFPE/PDMS mold cost/swelling.[27]	Incomplete products.[41,50] Time-intensive and secondary particles[40,46,59] Require specific stabilizer/surfactant and initiator choices[44,50] Size-limited.[57]	Heating above Tg or solvent/plasticizer softening and film stretching limitations[81,90] IIrregular shapes[83] Particle fusions[94] Rupture.[81,88] High-temperature curing.[102]	Clogging/sticking[97,103,105] Initiator concentration limitations.[100,103,105] Requires oxygen-inhibition edge effects.[110] Viscosity constraints[129,130]	Challenging isolation[117] Hours-long exposures.[119,123] Incomplete polymerization[124–126]

Table 1 (*continued*)

Field	2.1 Lithography	2.2 Seeded emulsion polymerization	2.3 Mechanical deformation	2.4 Microfluidic	2.5 Misc
Bio-Relevance	Protein photolithography reports biocompatibility and proteolytic degradability over weeks.[22] PRINT nanogels report low cytotoxicity in HeLa cells and were evaluated *in vivo* after IV injection[30] S-FIL PEG particles include enzyme-degradable peptide-crosslinked variants (Cathepsin B trigger)[38] "pelmeni" capsules combine polyelectrolyte multilayers with a biodegradable PLGA lid.[31]	Bio-derived starch nanoparticles were used as non-cross-linked seeds/stabilizers in a soap-free styrene system.[42] pH-responsive or reactive functionalization is explicitly reported in some systems.[59,68]	Biodegradable PLGA/PCL/PDLLA systems.[81,87,90,94] Artemether-loaded PLGA nanorods reported ≈90% THP-1 viability across 0.001–100 μg mL^{-1} and <10% haemolysis nanorods showed less haemolysis than nanospheres.[86] PLGA discs released encapsulated dye faster than microspheres in PBS (0.05% Triton X-100).[94]	PEGDA-based particles are presented as suitable for bioassays (graphical encoding and covalent incorporation of biomolecular probes protein conjugation).[106,108,110,114]	Alginate particles are explicitly positioned as biocompatible/biodegradable and were used for cell encapsulation.[131] sRBC platforms explicitly aim to mimic RBC deformability and use biocompatible/biodegradable PLGA templates limitations on PS biocompatibility are stated.[132]
Advantages	Compared to conventional polydisperse/spherical carriers, lithographic/templated approaches emphasize deterministic shape and monodispersity (*e.g.*, PDI ∼1 sharp edges/sidewalls).[22,30] PRINT nanogels were noted to maintain size/PDI at 37 °C *versus* a liposome comparator and to reduce PK confounding from polydispersity.[30] S-FIL release *via* PVA dissolution was highlighted as a gentler alternative to scraping/shear harvesting workflows.[38]	Seeded routes are repeatedly framed as maintaining monodispersity while enabling nonspherical/compartmentalized morphologies.[40,55] One-pot nonspherical hollow latexes were reported to improve hiding/opacity *versus* nonspherical solid particles.[41] Activated swelling protocols were described as producing nonspherical particles with excellent monodispersity and reproducibility.[59]	Deformation platforms are described as scalable/reproducible and enable high-aspect-ratio nonspherical particles from common spherical precursors.[81,89,90] Elongated PLGA discs showed higher adhesion than spheres.[85] Artemether-loaded PLGA nanorods reduced haemolysis relative to nanospheres.[86]	Microfluidic platforms emphasize narrow size distributions and continuous production (*e.g.*, 100–500 particles/s 5.6 × 10^6 particles per h).[100,110]	Several approaches emphasize access to nonspherical geometries without the use of molds or masks.[119,124,126] CDP is highlighted as rapid (seconds–minutes), solvent/template-free, and widely tunable in size.[124–127]
Throughput	∼10 000 particles in minutes (100 × 100 array)[22]	∼10^{10} particles per mL[61]	∼10^7–10^8 particles per hour[82]	12–36 particles per min[98]	CDP polymerization step is very fast (seconds; <45 s noted) and overall runs are minutes-scale[124,125]
	∼10^9 particles per exposure (6 in. wafer, 10 μm film; estimate)[25]	∼0.1 g particles per mL reaction mixture[70]	Roll-to-roll ∼10^8 particles in 1 mL from ref. 85	∼100–500 particles per s and ∼1.6 × 10^7 particles per h with 10-device chip[100]	∼4 × 10^5 particles per s[131]
	∼10^{10} particles per cm^2 per cycle[32]	∼10^8 micrometer-sized tetrahedral particles per batch[80]	∼10^8–10^{12} particles per run[89]	∼200–1000 particles per s[109]	
	∼1.97 × 10^6 particles per 17.35 cm^2 mold; yield 90.8 ± 1.9%[34]		Up to several grams of particles[84]	∼5.6 × 10^6 particles per h[110]	
	Up to ∼10^{12} or ∼4 × 10^{11} particles per 8-inch wafer[38]		2.5 × 10^9 particles[94]	∼400 000 particles per h[116]	
	Recovered mass example: 9.45 mg (PRINT nanogels radiolabeling run)[30]				

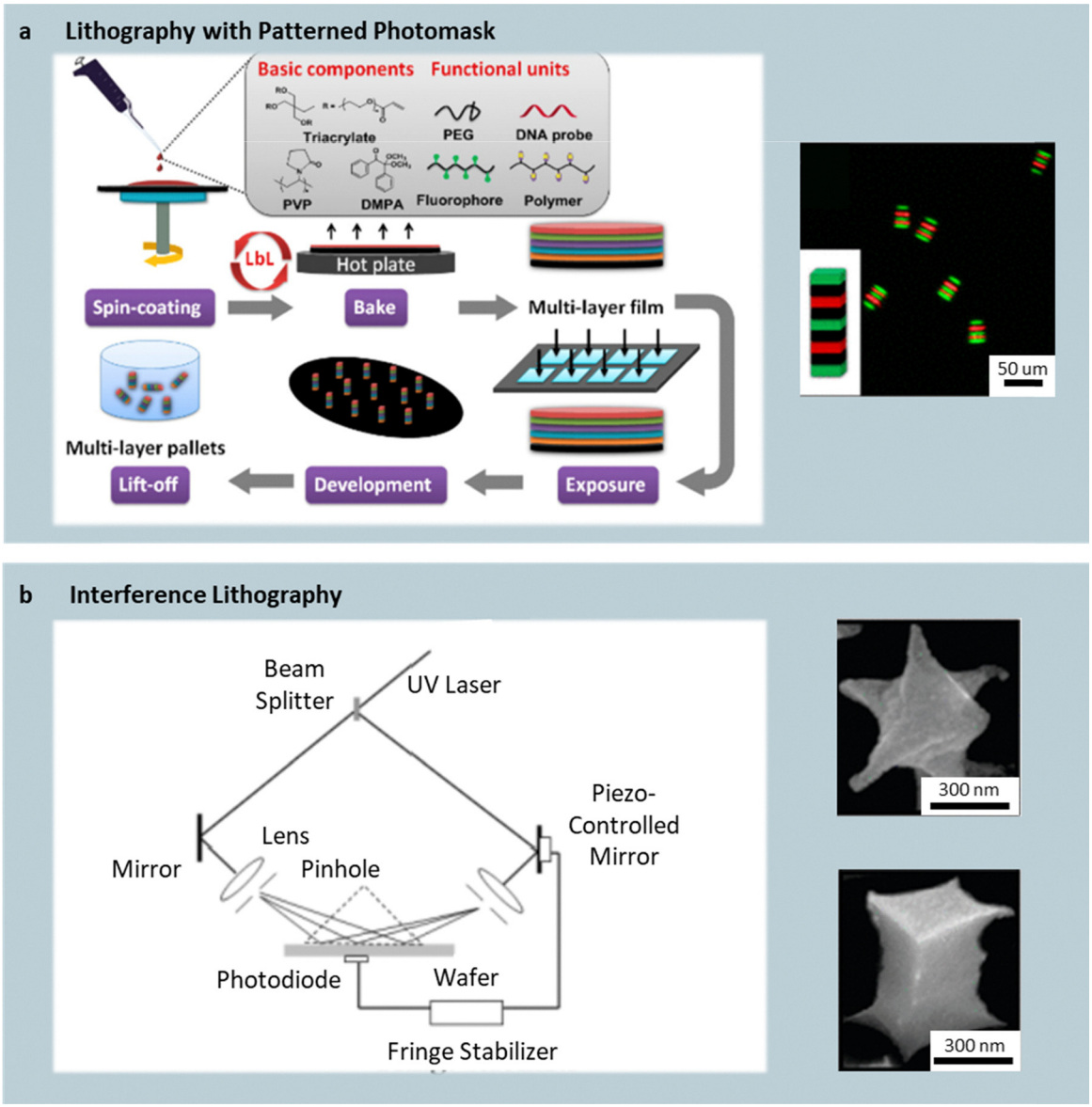

Fig. 1 Mask-based and maskless photolithography techniques. (a) Schematic of mask-based photolithography showing the steps of spin-coating of a positive photoresist, UV exposure through a photomask, and development of cuboid particles. Fluorescent micrograph of cuboid particles produced using this mask-based lithography technique. Reprinted from ref. 24 with permission from American Chemical Society, copyright 2016. (b) Schematic of interference lithography using intersecting laser beams to polymerize a photosensitive resin without a mask, forming complex 3D microstructures. Reprinted from ref. 23 with permission from Wiley, copyright 2007. SEM image of spinning-top-shaped and cuboid particles produced using interference lithography. Reprinted from ref. 25 with permission from American Chemical Society, copyright 2007.

is comparable to conventional photolithography—on the order of $\sim 10^9$ particles per single exposure on a six-inch wafer, likely a result of the limited UV penetration. Nevertheless, IL has been considered to afford more flexible 3D design freedom compared to conventional photolithography.

2.1.2. Template molding. Template molding fabrication generates nonspherical polymer particles, typically in the micrometer size range, by polymerizing formulations similar to those used in photolithography within cavities of patterned molds or the surface of pre-formed particles.[26–34]

Nonspherical polymer particles have been generated *via* hard-template replica synthesis, in which a pre-formed anisotropic particle serves as a sacrificial scaffold. In this approach, a non-spherical template, typically inorganic (*e.g.*, silica rods, cubes, hematite ellipsoids) or polymeric, is first synthesized independently. A polymer shell is then deposited onto the template surface through surface-initiated polymerization, layer-by-layer (LbL) assembly, sol–gel coating, or cross-linking of adsorbed macromers. Subsequent selective removal of the core (*e.g.*, by chemical etching, dissolution, or calcination) yields hollow or solid polymer replicas that preserve the original template geometry. This strategy has enabled polymeric replicas of rods, ellipsoids, cubes, dimpled particles, and lock-and-key geometries with high shape fidelity. For example,

silica templates have been used to produce polymeric colloids with well-defined multicavities.[35] Hollow silica and silica-polymer spheres (720–1000 nm) have also fabricated using LbL by sequentially depositing silica nanoparticles and polymer onto colloidal templates, followed by core removal *via* calcination or solvent decomposition. The wall thickness was tuned by adjusting the number of deposition cycles, while the final size and shape were dictated by the template morphology, yielding structures with potential applications in medicine, pharmaceutics, and materials science.[36] While this method offers excellent geometric fidelity and versatility across material chemistries, scalability depends on the availability and cost of the initial anisotropic templates and the efficiency of core removal. Nevertheless, hard-template replication represents a widely adopted and complementary route to nonspherical polymer particles, particularly for hollow capsules and biomimetic structures.

When template-molding is used, the mold is often fabricated using photolithography and subsequent transfer or replication steps, which dictates the in-plane geometry of the particles while cavity depth defines the out-of-plane dimension (Fig. 2a). Virtually any planar shape – triangle, donut, heart, or ring – can be realized, and stacked structures can be obtained *via* precise control over mold depth and multistep procedures (Fig. 2a(i–vi)).

A representative example is particle replication in non-wetting templates (PRINT), which employs a lithographically patterned silicon master to define a perfluoropolyether (PFPE) mold. A photoresist pattern is first generated *via* lithography and used as an etch mask to transfer the design onto a silicon wafer.[37] PFPE resin is then poured into the etched silicon cavities, cured, and peeled off to yield an elastomeric, non-wetting mold that reproduces the pattern. A polymer solution (*e.g.*, degradable poly(D-lactic acid), biocompatible polyethylene glycol (PEG), or proteinaceous solutions) is cast onto a delivery sheet and partially dried to form a thin film. This coated sheet is pressed against the PFPE mold under mild heat and pressure, allowing the softened polymer to flow into the cavities. A high-surface-energy harvesting substrate is then laminated on top; due to the PFPE's low surface energy, the filled cavities release the solidified particles when the harvesting substrate is lifted and later dissolved, freeing the molded particles (Fig. 2a).

In addition to thermal curing, UV-assisted molding provides a complementary route for forming nanoscale features.[38] For instance, step-and-flash imprint lithography (S-FIL) uses a quartz mold (transparent to UV light) patterned by high-resolution e-beam lithography, achieving feature sizes as small as 50 nm. The quartz mold is pressed onto a sacrificial PVA-coated silicon wafer coated with a UV-curable macromer (*e.g.*, PEG diacrylate or dimethacrylate of varying molecular weights). Upon UV exposure, the monomer mixture polymerizes within the mold cavities. Removing the quartz reveals patterned protrusions joined by a thin residual film, which is removed by brief oxygen plasma etching. Dissolving the PVA layer releases the shaped nanoparticles (Fig. 2a(vii and viii)).

Template molding can also produce polymer cholesteric liquid crystal (PCLC) flakes with engineered optical properties for sensing or display applications. In one example, a PDMS mold replicated from a photoresist master is spin-coated with a thin PVA layer, then filled with a liquid-crystalline mixture containing diacrylates, monoacrylates, and chiral dopants. UV curing, followed by PVA dissolution, releases the PCLC flakes.[39] Adjusting spin-coating speed precisely controls the PVA thickness and thus the final flake height, which is the difference between the molded height (10 μm in this case) and PVA thickness. A PVA coating obtained at 500 rpm yields a PVA thickness of ~2 μm and thus flake heights of ~8 μm, while 2000 rpm produces a PVA thickness of ~0.5 μm, and thus ~9.5 μm flakes, enabling tunable optical responses *via* controlled film thickness.

Lithography and template molding both deliver excellent shape fidelity and narrow size distribution, making them especially suitable for applications requiring rigorous dimensional control. However, scalability remains limited by planar processing throughput and mold-fabrication costs. Even small changes to the particle shape or size require remaking of the mold, making each design-to-test iteration laborious and costly. The achievable particle size is ultimately constrained by lithographic resolution, and true three-dimensional freedom is limited unless interference or multilayer approaches are employed. Despite these constraints, template molding provides a robust, reproducible path to nano- and microscale particles with diverse geometries and well-defined chemistries—an indispensable complement to photolithographic platforms.

2.2. Seeded emulsion polymerization

Seeded emulsion polymerization extends the classical emulsion polymerization framework to produce nonspherical polymer particles through polymerization-induced phase separation (PIPS).[40–54] The process begins with narrowly dispersed seed particles, typically polystyrene (PS) or poly(methyl methacrylate) (PMMA), prepared *via* standard emulsion polymerization. Those seed particles are redispersed into a second emulsion containing fresh monomer, often accompanied by plasticizers, crosslinkers, or swelling agents. The monomer diffuses into and swells the seed particles. Upon initiation of its polymerization, a secondary polymer network forms inside the seed particles, often with a positive free energy of mixing (*i.e.*, $\Delta G_{mix} > 0$), hence driving phase separation between the growing and pre-existing polymers. At the same time, chain mobility, determined by the relation between the reaction temperature and the glass-transition temperature (T_g), governs how far the phases can migrate before the matrix vitrifies. High chain mobility ($T \gg T_g$) favors complete rearrangements, such as core–shell structures that often retain their overall spherical shape, whereas limited mobility locks transient domains into kinetically trapped nonspherical shapes. By tuning seed rigidity, monomer polarity, plasticizer content, inhibitor concentration, and swelling rate, each recipe can be positioned at a unique point on the thermodynamic-kinetic landscape, unlocking lobed, indented, Janus, and porous architectures. While emulsion polymerization is industrially relevant, there have been limited examples of scaled production of seeded emulsion

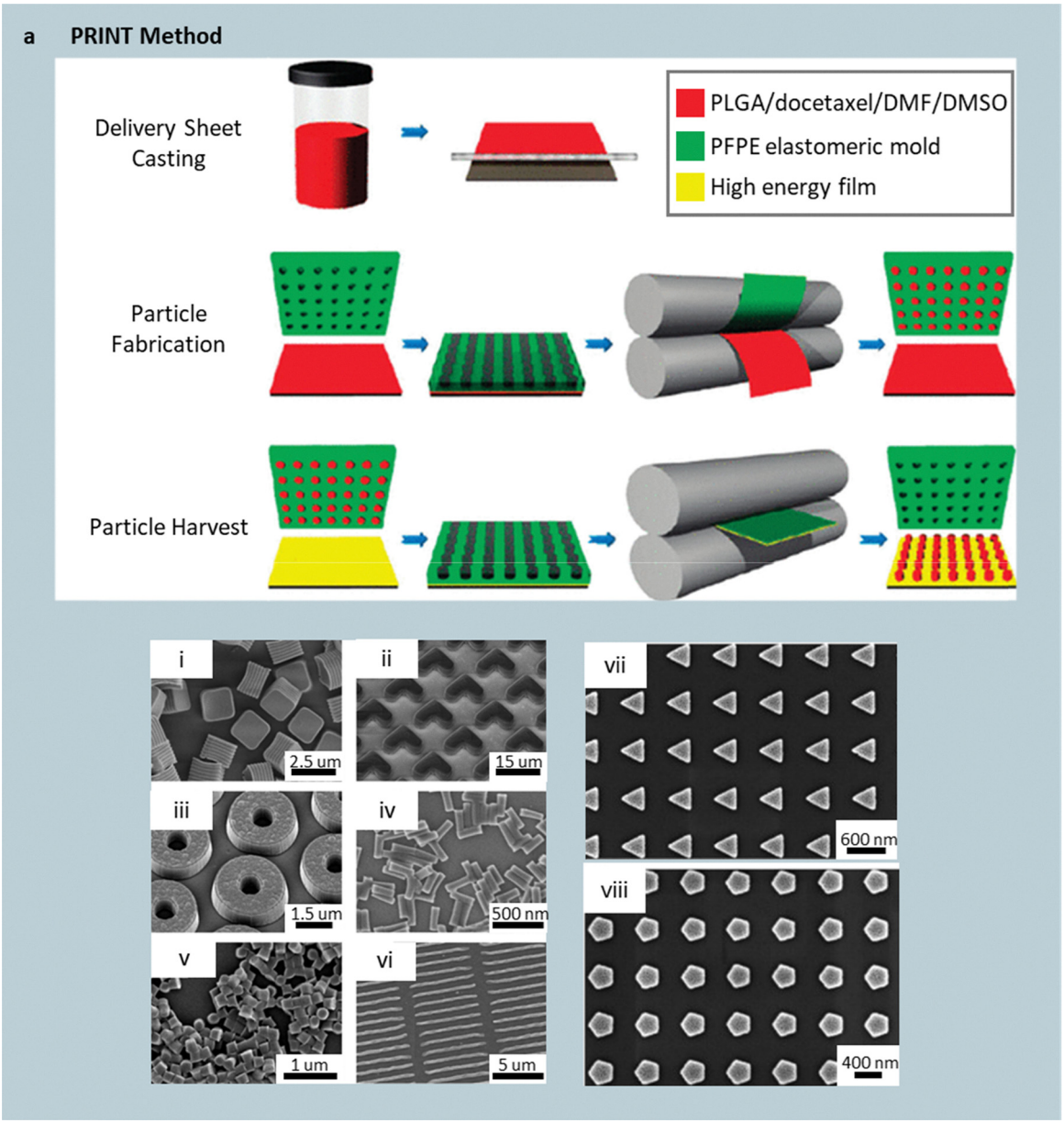

Fig. 2 Template molding fabrication. Schematic of particle replication in non-wetting templates (PRINT) technique, comprising the steps of solution casting onto a delivery sheet, pressing the delivery sheet (red) against a patterned perfluoropolyether (PFPE) mold (green) using a heated roller to fill the mold with the particle-making material, pressing a harvesting substrate (yellow) against the filled mold using a heated roller to transfer the particles to a soluble substrate. PRINT has enabled particle shapes including (i) cuboids, (ii) boomerangs, (iii) rings, (iv) long cylinders, (v) short cylinders, and (vi) rods. Reprinted from ref. 26 with permission from American Chemical Society, copyright 2011. Step-and-flash imprint lithography (S-FIL) using a quartz mold pressed against a sacrificial PVA- and UV-curable precursor-coated wafer yields (vii) triangular and (viii) pentagonal particles after UV curing and PVA dissolution. Reprinted from ref. 38 with permission from Elsevier, copyright 2007.

polymerization, likely due to inconsistent particle morphology and properties[55]

2.2.1. Monomer-driven swelling. In monomer-driven swelling, secondary monomers penetrate the seed and trigger PIPS during polymerization, sculpting lobed or indented geometries. Seed crosslink density, rigidity, and swelling ratio critically determine whether phase separation occurs within, on, or beyond the seed surface.

A representative example employs γ-ray polymerization of poly(styrene–divinyl benzene–acrylic acid) (p(S-DVB-AA)) seeds with 3-(methacryloxy)propyl-trimethoxysilane (MPS) and styrene (co-solvent).[56] Varying styrene concentration modulates MPS solubility in the crosslinked seed and shifts the morphology sequence from raspberry-like (low styrene and small MPS domain size) to Mickey-Mouse (intermediate) to snowman-like (high styrene and large MPS domain size) particles (Fig. 3a). Similar lobed structures can be achieved using PMMA seeds at low reaction temperatures, where limited chain mobility confines polymerization to the seed surface, giving rise to raspberry-like particles.[57] Subsequent annealing merges adjacent lobes as

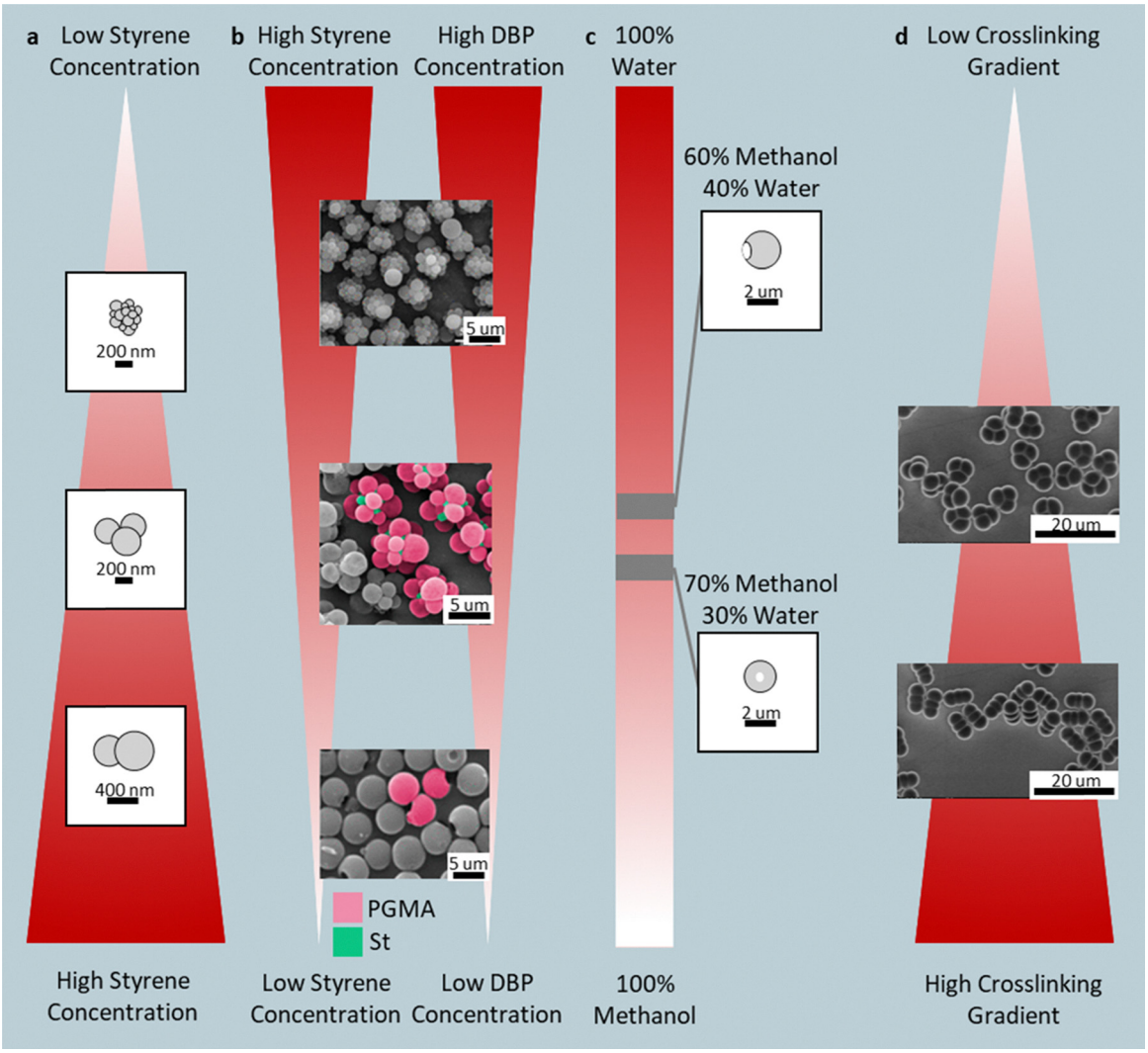

Fig. 3 Monomer-driven swelling shapes: (a) raspberry, Mickey-Mouse, and snowman *via* styrene-MPS swelling of P(S-DVB-AA) seeds; (b) pineapple-, cluster-, and single-dimpled morphologies from PS/DBP swelling. Reprinted from ref. 58 with permission from American Chemical Society, copyright 2016; (c) single-dimpled and donut particles *via* APS-mediated water inclusion; (d) trimers, rods, and snowmen from multi-stage DVB gradients. Reprinted from ref. 60 with permission from Wiley, copyright 2007.

interfacial tension drives domain coalescence, reducing total polymer–water interfacial energy.

Uncrosslinked seeds can also yield complex shapes. In one example, uncrosslinked poly(glycidyl methacrylate) (PGMA) seeds were partially swollen with dibutyl phthalate (DBP) and styrene.[58] The swollen outer layer underwent phase separation, forming DBP-rich droplets that protrude from the seed surface. Upon seed removal (likely by centrifugation) from the swelling environment, the seeds are redispersed back into water, and the DBP diffuses back into the continuous phase; the protrusion pinches off, imprinting dimples on the PGMA seed. Next, these dimpled PGMA seeds are again swollen with controlled ratios of DVB, S, and azobis(isobutyronitrile) (AIBN). Polymerization leads to various-sized and numbers of PS protrusions. Adjusting DBP and styrene ratios produces pineapple-like (high DBP and St), cluster-like (moderate DBP and St), or single-dimpled spheres (low DBP and St) (Fig. 3b)

Reaction additives further enrich the morphology diversity. While the polymerization of a methacrylate mixture containing methyl methacrylate (MMA), glycidyl methacrylate (GMA), and ethylene glycol dimethacrylate (EGDMA) in PS seeds give rise to spherical particles, with a polymethacrylate shell and a PS core, the addition of inhibitors, such as 4-methoxyphenol (MEHQ) or dissolved O_2 can slow the methacrylate polymerization to allow time for the shell to densify as the crosslinking density increases.[59] That densification leads to a compressive mismatch between a rigid P(MMA–GMA–EGDMA) shell and a soft PS core, resulting in wrinkled raisin-like morphologies at methacrylate-to-PS mass ratios of 15–20. At mass ratios of 60, the seed absorbs far more monomer. Here, during polymerization, phase separation of the highly crosslinked region grows into a hemispherical shape while pushing into and greatly compressing the PS phase into a flat region, generating an acorn-like Janus particle. Introducing hydrophilic swelling

agents such as ammonium persulfate (APS) draws water into the seed, forming trapped droplets that collapse into singular dimples or central voids upon drying.[60] To control the particle morphology precisely, the polarity of the continuous phase can be adjusted by mixing methanol and water. Tuning the methanol-to-water ratio from 60/40 to 70/30 changes the droplet size, transitioning the particle morphology from single-dimpled spheres to donut-like particles (Fig. 3c).

Sequential emulsion polymerization steps can further encode asymmetry. For instance, PS seeds ($\sim$1.5 μm) are first swollen and crosslinked in styrene with DVB, producing symmetric dimers.[61] A second swelling step deliberately imposes a crosslinking-density gradient between the two bulbs by varying the DVB dose, establishing a tunable elasticity contrast that biases subsequent growth. In a third swelling, additional monomer and toluene are introduced; upon polymerization, morphology follows the preset gradient (Fig. 3d). Low elasticity contrast permits slow, near-isotropic monomer transport, yielding orthogonal triangular trimers. Intermediate contrast focuses growth at the softer bulb, producing linear three-bulb rods. At high contrasts, the more rigid bulb resists swelling while the softer bulb swells easily, suppressing new lobe formation and freezing the particle as a snowman-like dimer.

2.2.2. Hydrocarbon-swollen seeds. Unlike monomer-driven swelling, hydrocarbon swelling introduces physical deformation mechanisms.[62] Here, hydrocarbons diffuse into the seed particle, temporarily plasticizing it; upon evaporation, the seed collapses or buckles, creating concave or porous morphologies. When combined with reactive monomers, the hydrocarbon-treated domains act as transient templates for more complex shapes, *e.g.*, wiffle-ball, Pac-Man, and saucer.

For example, seeded emulsion polymerization using uncrosslinked PS seeds swollen with 2-ethylhexyl methacrylate (EHMA) and hydrocarbon leads to particles that deform into predictable shapes upon solvent removal.[63] Longer-chain hydrocarbons (*e.g.*, dodecane, 12-carbon backbone) induce limited swelling, producing polyhedral particles, whereas shorter-chain hydrocarbons (*e.g.*, hexane, 6-carbon backbone) enable greater deformation, yielding progressively flatter, saucer-like morphologies. Introducing PMMA particles as secondary seeds (*i.e.*, dual-seeded emulsion polymerization) alters the polarity of the local environment, causing EHMA/hydrocarbon droplets to nucleate on regions of the PS seed farthest away from neighboring PMMA seeds, resulting in asymmetric swelling (Fig. 4a). This asymmetric swelling was observed with lower-affinity hydrocarbons to PS, such as dodecane. The dodecane nucleates on the PS seeds farthest away from the PMMA seeds, grow, and the subsequent PEHMA/hydrocarbon extraction (*via* 1-butanol), produced a bowl-shaped structure. Conversely, when hexane is used, its enhanced swelling capacity offsets the polarity imbalance caused by the PMMA seeds, thereby mitigating swelling asymmetry and nucleating evenly across the PS seed. After growth and extraction of the PEHMA/hydrocarbon domains, pits are left behind, forming a "Wiffle-ball-like" particle.

Complete dissolution of the seed may also unlock new shapes. When PS seeds are pre-swollen with 1-chlorodecane (in water) and then an oil phase (acrylic acid (AA)) emulsion consisting of styrene (S), divinylbenzene (DVB), sodium dodecyl sulfate (SDS), and AIBN is added, an emulsified droplet containing untangled PS chains is achieved.[64] Once polymerization begins, the dissolved PS chains adsorb onto the nascent poly(styrene-*co*-divinylbenzene) (PSDVB) nucleus and sterically block the nucleus's internal propagation sites. Due to acrylic acid (AA) being hydrophilic, contact with the nuclei confines propagation to the oil–water interface. The hydrophobic PS chains, in turn, retreat from this interface, shielding the interior nucleus while leaving reactive sites exposed at the boundary, resulting in preferential growth along the interface. Increasing the mass of dissolved PS (*i.e.*, dissolving more seeds) increases site shielding, driving more polymerization at the interface. For example, an open-mouth Pac-Man-like particle (Fig. 4b) was achieved at a high concentration of dissolved PS due to extensive interior propagation site shielding, inhibiting polymer growth at the core of the droplet and preferential growth around the perimeter. Whereas when the concentration of PS chains is decreased, fewer internal propagation sites are shielded, resulting in increasingly more polymer being formed in the core, causing the Pac-Man mouth to progressively close.

Core–shell seed designs provide additional shape control. PS/poly(styrene-*co*-sodium styrene sulfonate (P(S-NaSS)) core–shell particles swollen with *n*-butyl methacrylate (*n*-BMA) and Dodecane yield dodecahedral or golf-ball-like morphologies depending on the shell thickness and PS molecular weight (Fig. 4c).[65] Thinner shells and lower PS molecular weight enable the swollen *n*-BMA/dodecane domains to coalesce more readily. After polymerization, the composite particles were isolated by repeated centrifugation and methanol washing, then air-dried at room temperature. During drying, evaporation of Dodecane causes volumetric shrinkage of the few large P(*n*-BMA)/dodecane domains, driving interfacial-tension-induced collapse of the shell into a faceted, polyhedral structure. Conversely, seeds with thicker or higher-molecular-weight shells restrict domain coalescence, forming numerous smaller P(*n*-BMA)/dodecane domains; upon evaporation, shrinkage of these domains produces the characteristic golf-ball-like dimpling is synthesized. Similarly, silica-nanoparticle-coated PS seeds swollen with decane produce "bitten-apple"-shaped particles approximately 500 nm in diameter with up to 150 nm 'bite sizes' (Fig. 4d).[66]

During dispersion polymerization to create the PS–SiO_2 seeds, 22 nm methanolic silica colloids electrostatically interact with the cationic initiator, 2,2′-azobis(isobutyramidine) dihydrochloride (AIBA).[67] In conjunction with the low repulsive forces between silica nanoparticles, this interaction promotes the formation of a densely packed, contiguous silica-rich surface on the PS particles. During the shaping step, decane is added to a 9 : 1 methanol/water medium that partitions preferentially into the PS core because (i) decane is only sparingly soluble when water is present, and (ii) the permeable yet mechanically robust silica shell aids the particle in resisting deformation, leading to the formation of a single decane-rich bulge. As the suspension cools, decane evaporates more rapidly than the plasticized PS can relax, causing the silica shell to

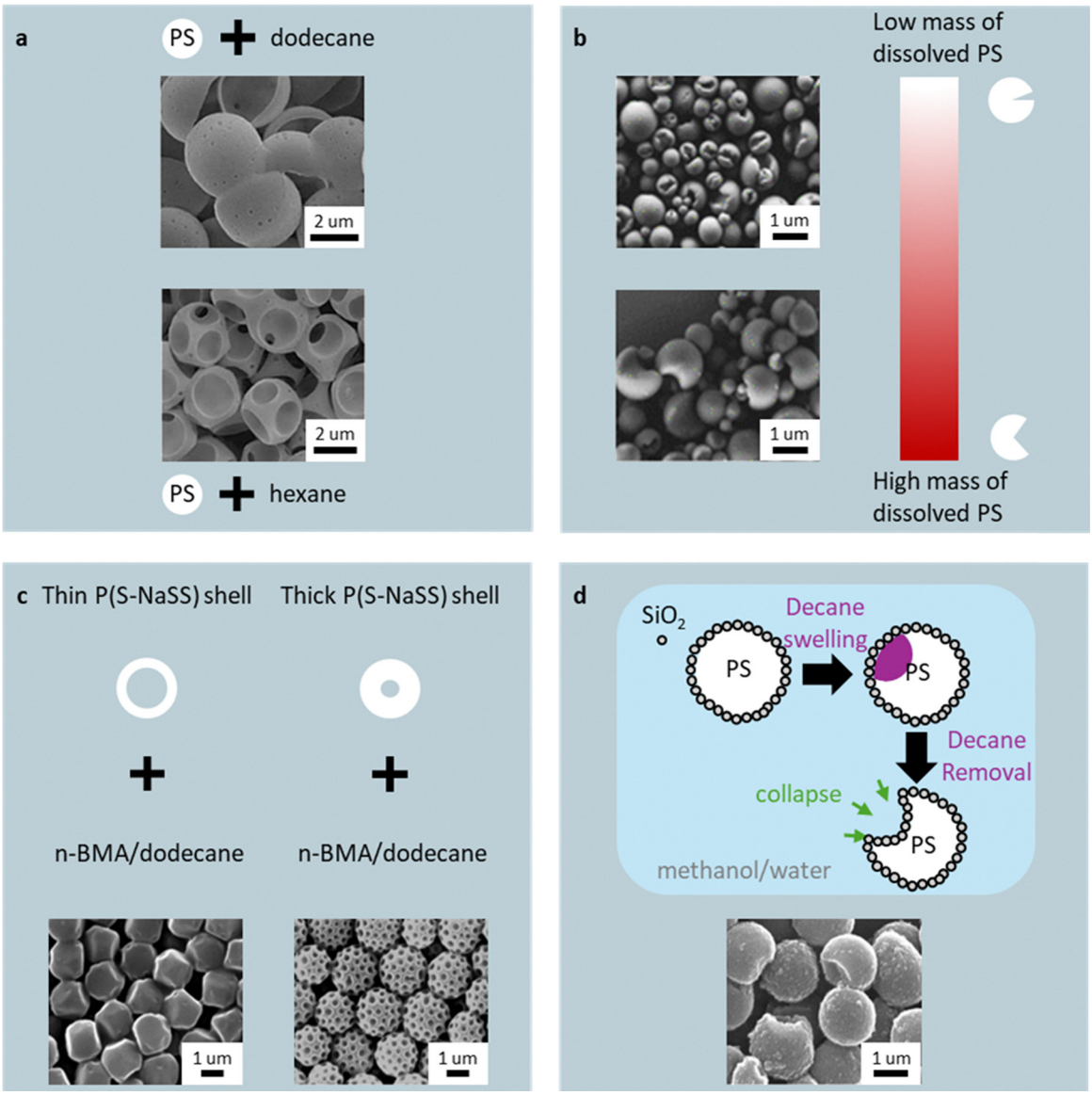

Fig. 4 Hydrocarbon-swelling routes: (a) bowl and wiffle-ball morphologies from dodecane/hexane swelling. Reprinted from ref. 63 with permission from Springer, copyright 2012; (b) Pac-Man-like cavities from dissolved PS seeds. Reprinted from ref. 64 with permission from American Chemical Society, copyright 2018; (c) dodecahedral and golf-ball-like shapes from core–shell PS/P(S-NaSS) seeds. Reprinted from ref. 65 with permission from The Society of Polymer Science, copyright 2010; (d) bitten-apple PS–SiO_2 particles. Reprinted from ref. 66 with permission from American Chemical Society, copyright 2018.

collapse and leave one deep crater—the characteristic ''bitten-apple'' shape.

2.2.3. Sacrificial phases. Sacrificial domains, *i.e.*, transient phases that are later removed, or seed-guided geometric confinement, provide an orthogonal lever to PIPS, enabling voids, hollows, flat facets, and otherwise hard-to-access curvatures.[68–74] In practice, a removable phase first sculpts the internal/external topology during swelling and polymerization; selective dissolution or extraction then ''develops'' the final geometry. Separately, pre-assembled seed packings can confine a liquid precursor into polyhedral cavities, yielding pyramids or concave-faced cubes.

Post-PIPS removal can imprint surface texture by selectively dissolving the sacrificial polymer while leaving the matrix intact. Uncrosslinked PGMA microspheres (4–8 μm in diameter) have been swollen with DBP in the presence of styrene (for 24 hours at 40 °C).[75] Upon AIBN-initiated polymerization at 80 °C, the styrene polymerizes, giving rise to buds that nucleate and coarsen on the PGMA surface to produce raspberry-like clusters (Fig. 5a). A rapid (20 seconds) rinse in 85–95 vol% THF/H_2O dissolves PS but swells PGMA, lifting the buds and a thin subsurface layer to leave ''golf-ball'' dimpling (Fig. 5a). The selective removal of PS can be explained using the Hildebrand solubility parameter (δ), as THF and PS have comparable δ's, which differ from PGMA. Similarly, programming the interfacial tensions of the two polymer phases against water prescribes whether hemispheres develop convex, flat, or concave bases (Fig. 5b). Uncrosslinked PS seeds ($\sim$1 μm in diameter,

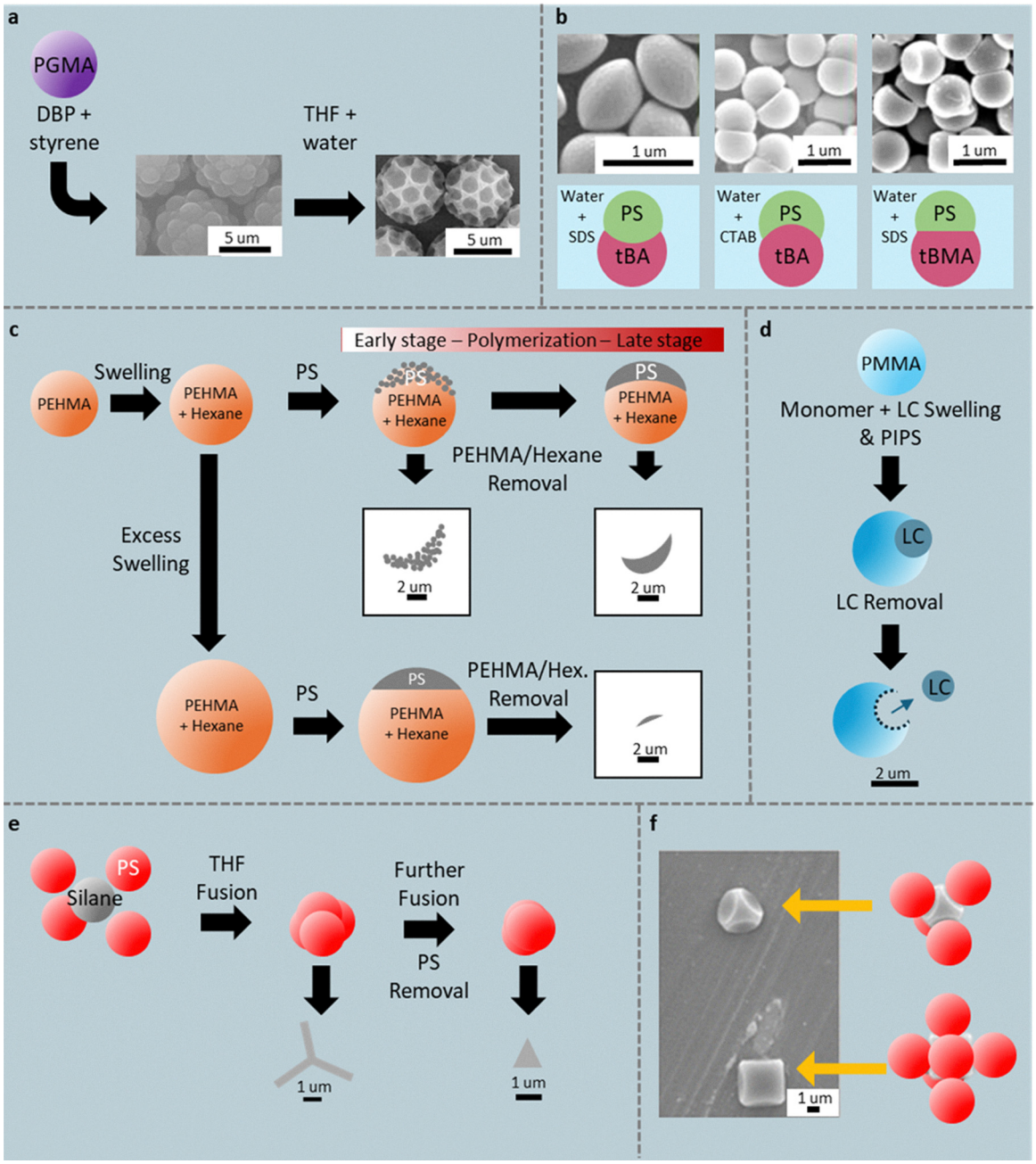

Fig. 5 Sacrificial-phase and confinement routes to voided spheres, hemispheres, bowls, helmets, Y-shapes, pyramids, and concave-faced cubes. (a) PGMA-PS raspberries made by PIPS. Reprinted from ref. 75 with permission from American Chemical Society, copyright 2024; (b) golf balls made by selectively dissolving PS with a rapid rinse using THF/H_2O. (c) Hemispheres with convex, concave, and flat bases *via* control over the interfacial tension. Reprinted from ref. 76 with permission from American Chemical Society, copyright 2017. (c) PHEMA/hexane routes to porous bowls and thick shells; saucers at high hexane content. (d) LC-templated PMMA helmets; (e) Y-shapes and pyramids from fused PS clusters. (f) TPM droplets polymerized in tetrahedral or octahedral colloidal cages formed by PS particles. Reprinted from ref. 80 with permission from American Chemical Society, copyright 2017.

plasticized with toluene) have been swollen with a sacrificial (meth)acrylate in the presence of a surfactant, giving rise to Janus particles after PIPS.[76] With *tert*-butyl acrylate (*t*BA) and sodium dodecyl sulfate (SDS), the *t*BA–water tension is slightly lower than the PS–water tension, so the p*t*BA phase partially engulfs the PS phase, reducing the PS surface area in contact with the water. Dissolving the p*t*BA reveals PS hemispheres with a convex base. Keeping *t*BA but replacing SDS with cetyltrimethylammonium bromide (CTAB) lowers the PS–water tension below the *t*BA–water tension (due to better affinity to the PS); the higher-energy p*t*BA interface now bulges into the PS phase, and dissolving it leaves a concave base. Interfacial tensions were calculated by measuring the contact angle of water containing CTAB or SDS atop thin films of either polymer. Switching the monomer to *tert*-butyl methacrylate (tBMA) in SDS lifts that sacrificial-polymer tension almost to parity

with the PS–water value, leaving neither phase favored. Hence, no bulge, thus, the internal boundary between the two polymers is flat, and removing the sacrificial half yields a flat-based hemispherical PS particle.

Combining hydrocarbons with a sacrificial phase or using an inert liquid-crystal droplet also expands the accessible bowl and shell morphologies. Moderately hexane-swollen PEHMA seeds have been shown to maintain sufficient rigidity to support the asymmetric formation of PS domains that coalesce and, upon PEHMA sacrifice, a porous bowl/shell is formed (Fig. 5c).[77] The asymmetric precipitation is caused by dominant St uptake by the PS oligomers that nucleate first on the PEHMA particle. Further polymerization back-fills pores to thicken the shell (Fig. 5c). Excess hexane greatly enlarges the PEHMA seed, and the PS domain then forms a small cap sitting on a larger sphere leading to a flat, saucer- or disc-like morphology (Fig. 5c). Alternatively, a single E7 liquid-crystal droplet can be pushed outward from crosslinked PMMA seeds, swollen by styrene, MMA, and E7, during PIPS; methanol extraction of E7 leaves hollow helmet-like microcapsules stabilized by the crosslinked matrix (Fig. 5d) Here the shaped particle is meant to hold the LC, giving rise to controlled electro-optical particle properties; however, LC removal yields shaped polymer particles.[78]

Finally, geometric confinement imposed by pre-arranged seed packings acts as a colloidal mold that fixes otherwise in accessible polyhedral shapes. Partial THF-induced fusion of tetrahedral PS clusters lets a polymerizable silane oil ((3-glycidyloxypropyl) trimethoxy silane and 3-(trimethoxysilyl)propyl methacrylate) extrude through interstices and be trapped mid-transit on curing, giving Y-shaped hybrids (Fig. 5e); complete fusion closes interstices and yields pyramidal particles.[79] Similarly, compressing monodispersed PS colloids creates tetrahedral clusters and octahedral cages that are capillary-wetted with 3-methacryloxypropyltrimethoxysilane (TPM) droplets.[80] *In situ* polymerization produces smooth-edged pyramids (in tetrahedral sites) and concave-faced cubes (in octahedral sites) in the same batch (Fig. 5f).

2.3. Mechanical deformation

Mechanical routes can reshape pre-made spherical particles, typically PS, PMMA, PLGA, or poly(ε-caprolactone) (PCL), into anisotropic shapes by softening the polymer (heat or solvent) and imposing shear, tensile, or compressive strain. Most methods highlighted here utilized feedstock particles ranging from a few hundred nanometers to tens of microns. Overall, these methods incorporate relatively inexpensive tools and straightforward processes to deliver large numbers of shape-controlled particles, although strain heterogeneity can lead to shape dispersity, and the frequent need for high temperature or plasticizing solvents further reduces the batch-to-batch reproducibility.[81,82] Fundamentally, shapes emerge from three coupled levers: viscosity of the polymer melt that constitutes the particle (set by T–T_g and solvent uptake), interfacial wetting with the embedding matrix, and the spatial uniformity of the applied strain field. Basic operations, such as stirring a suspension of PS particles in the presence of plasticizers (*e.g.*, 2 wt% PVP), yield rods and ellipsoids.[83,84] Judicious control over viscosity and wetting, as detailed below, further expands the library to discs, barrels, bullets, UFOs, and facetted polyhedral (Fig. 6 and 7).

2.3.1. Film stretching. In film-stretching (Fig. 6b), spheres are embedded in a polymer film (*e.g.*, PVA film, plasticized with 2 wt% glycerol), then deformed under controlled temperature/solvent and strain.[85–88] After cooling, the film matrix can be dissolved to release the shaped particles. Two common methods are liquefying the particles (*e.g.*, by heating them above the T_g or solvent immersion) and then stretching the matrix (herein referred to as Scheme A), or stretching followed by liquefying (Scheme B).[89]

In Scheme A, particle shape is governed by the particle size, particle viscosity (after liquefying), and film thickness (Fig. 6a). At 120 °C, a ∼2× uniaxial draw of spheres (∼2 μm in diameter) in a 70 μm film produces rods (Fig. 6a(i)), while the same temperature in a thinner, 35 μm film flattens particles (∼1 μm in diameter) into rectangular disks (Fig. 6a(ii)). Here, thinner films leads to the production of flatter particles due to strong particle association with the film arising from hydrogen bonding. Heating the particles to 140 °C lowers viscosity and enables skinny worm-like particles (Fig. 6a(iii)). Replacing heat with toluene further depresses viscosity; a 5-fold draw of particles (∼2 μm in diameter) embedded in a 35-μm film yields ultrathin elliptical disks (tens of nm thick) (Fig. 6a(iv)), which become porous when quenched directly into IPA (as solvent extraction outpaces chain relaxation; Fig. 6a(v)). Larger feedstock particles (∼6 μm) bias toward UFO-like caps, likely due to the limited plasticization at the center of the particle. Symmetric 2D strain gives oblate ellipsoids. Smaller feed particles (∼200 nm in diameter), upon toluene liquefaction, produce flat circular disks due to the more complete deformation compared to larger particles.

In Scheme B, the film is stretched while particles remain glassy, creating ellipsoidal voids that are then filled upon softening; shape is governed by both viscosity and particle–film wetting (Fig. 6c). At 130 °C, PS particles (∼3 μm in diameter) in a 35 μm film remain viscous (cP not reported) and thus partial void filling, yielding barrels (Fig. 6c(i)); slightly lowering viscosity drives asymmetric wetting at 140 °C favoring bullet shape (Fig. 6c(ii)). With toluene, viscosity is further lowered, causing uniform filling yielding pills (1D draw; Fig. 6c(iii)), while 2-fold (biaxial draws form pulleys and biconvex lenses, from ∼10 μm and ∼1 μm particles, respectively (Fig. 6c(vi and v)).

In addition, alternating Schemes A/B and changing draw axes generate wrinkled ellipsoids (Fig. 6d(i and ii)), ribbons (Fig. 6d(iii)), bicones (Fig. 6d(iv)), tacos (Fig. 6d(v)), and other hybrids. Typical lab batches yield 10^8–10^{12} particles (1–30 μm). Further strain-field engineering and automation are possible. An eight-clamp stretcher (equipped with an oil bath) creates deliberate strain heterogeneity in one pass—central true-biaxial zones form discs; inter-clamp uniaxial corridors produce rods; near-clamp regions give ellipsoids—useful for rapid generation

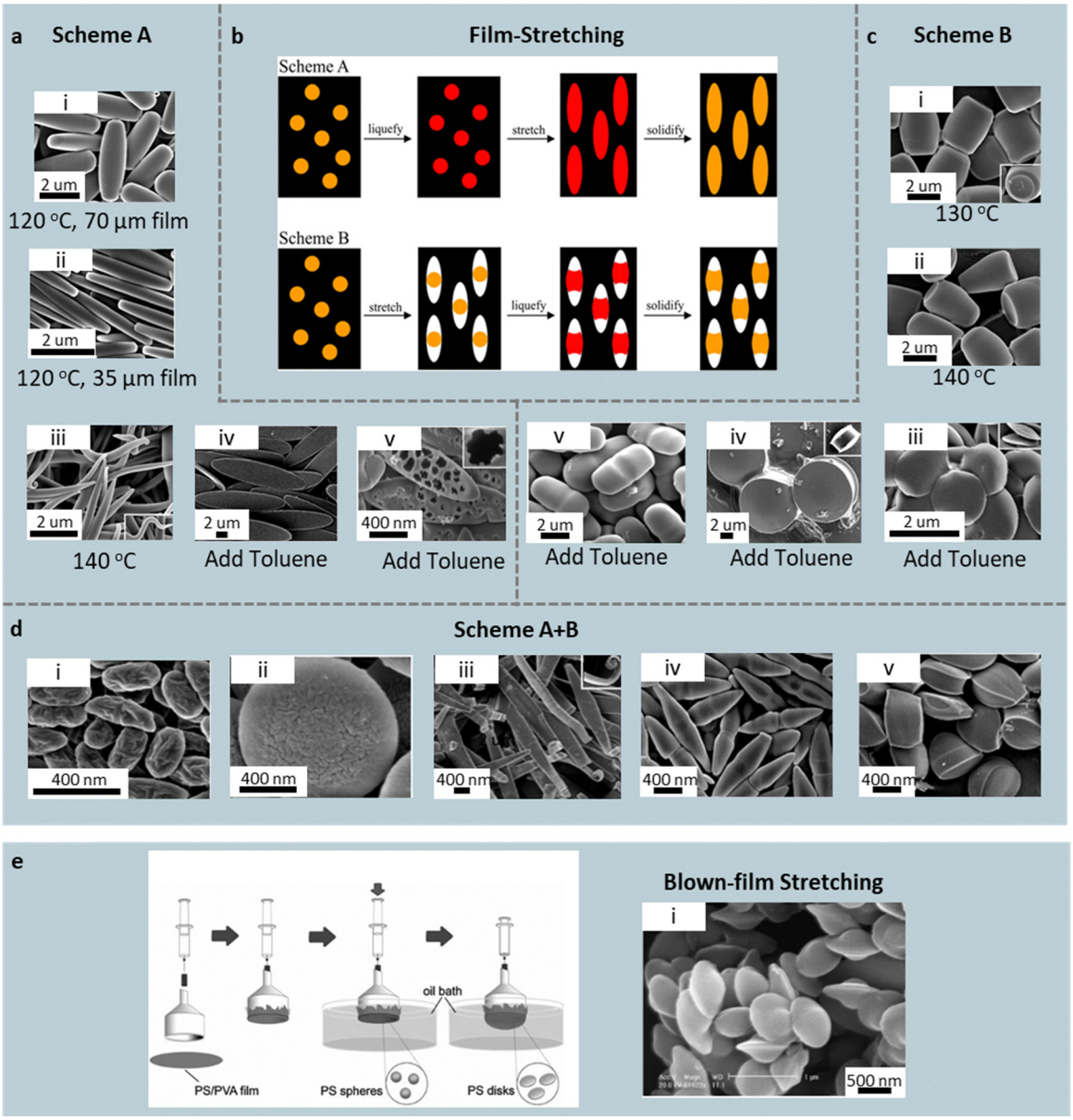

Fig. 6 Film-stretching routes to anisotropic polymer particles. (b) Schematic of two film stretching methods: (a) Scheme A (liquefy, stretch, solidify) and (c) Scheme B (stretch, liquefy, solidify), for spheres embedded in a polymer film. Scheme A: (a-i) rods from a 70-µm film at 120 °C, (a-ii) flat rectangular disks from a 35-µm film at 120 °C, and (a-iii) worm-like particles at 140 °C. Using toluene instead of heat yields (a-iv) elliptical disks, which become (a-v) porous when quenched into IPA. (c) Scheme B: (c-i) barrels at 130 °C and (c-ii) bullets at 140 °C. With toluene: (c-iii) pill-shaped particles under 1D draw; (c-iv) pulleys (c-v) and biconvex lenses under moderate and strong biaxial draw, respectively. (d) Combining schemes yields (d-i, ii) wrinkled ellipsoids, (d-iii) ribbons, (d-iv) bicones, and (d-v) tacos. Reprinted from ref. 89 with permission from National Academy of Sciences, USA, copyright 2007. (e) Schematic of the blown-film stretching method, which produces (e-i) UFO-like particles from PS/SiO_2 particles. Reprinted from ref. 91 with permission from Wiley, copyright 2008.

of libraries of intrinsically shape-polydisperse particles. In addition to PS, poly(lactic-*co*-glycolic acid) (PLGA) and poly-(ε-caprolactone) (PCL) microparticles have been used as feedstock.[90] Blown-film stretching distributes tension more uniformly: a heated, particle-laden membrane is inflated over a 50-mm funnel, narrowing the size/shape distribution of ellipsoidal particles made of PVA or PS (Fig. 6e).[91] Using this method, PS/SiO_2 core–shell particles adopt UFO morphologies under higher inflation (Fig. 6e–i). For heat-sensitive cargo, low-temperature (≈50 °C) biaxial stretching of chitosan-grafted poly(isobutyl cyanoacrylate) (PIBCA) nanoparticles generates lemon-like drug-carrier particles with mucoadhesive shells.[92]

It is important to note that while throughput scales with particle loading in the film, increasing loading could induce contact and shape distortion. Automation (servo grips in a temperature-controlled chamber) reduces film tearing and improves run-to-run reproducibility; however, as with all stretching, it cannot eliminate strain gradients entirely.

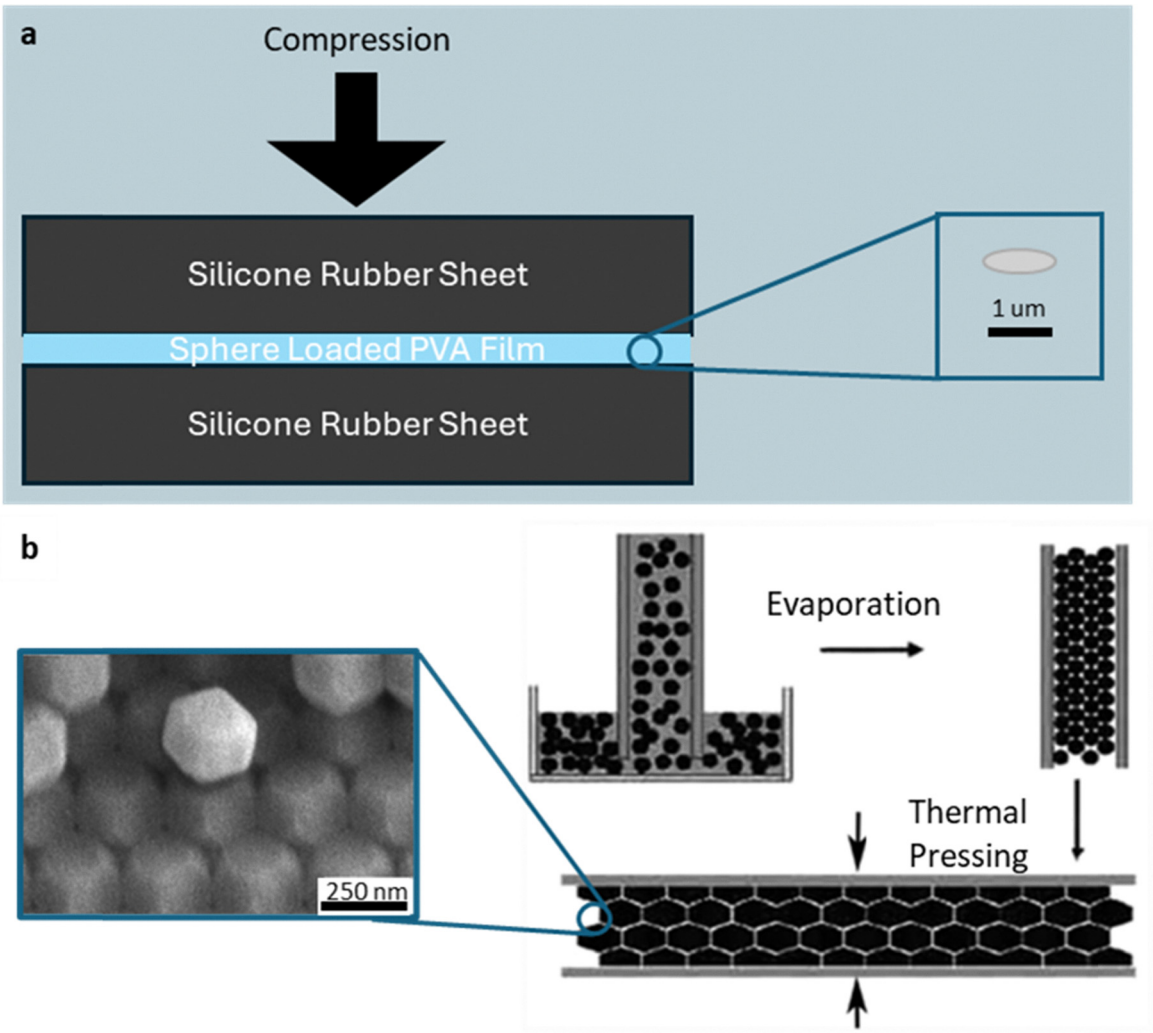

Fig. 7 Compression-based shaping of polymer particles. (a) Film squeezing method: schematic showing PVA film embedded with PS spheres compressed between two elastic sheets at elevated temperature to induce biaxial deformation. Resulting monodispersed disc particles after cooling and film dissolution. (b) Thermal pressing of packed lattices: schematic illustrating close-packed polymer spheres confined between glass slides, heated slightly below T_g, and compressed to form faceted particles. Resulting polyhedral particles by thermal pressing. Reprinted from ref. 96 with permission from American Chemical Society, copyright 2005.

2.3.2. Compression. Compression imposes more uniform strain than tensile drawing and therefore reduces shape heterogeneity within one batch. Film squeezing (biaxial compression, Fig. 7a), for example, creates monodisperse disc particles using a micron-thick PVA film loaded with PS spheres (~0.5, 2, 4 μm in diameter).[93] The film is sandwiched between silicone rubber pads (millimeter thick) to ensure that the film experiences purely biaxial extension during compression, compressed at 135 °C, and cooled under load. The aspect ratio of the as-produced disk particles is controlled by the applied compression. The method is straightforward, but largely limited to discoidal geometries.[94,95]

A complementary approach, thermal pressing of packed lattices (Fig. 7b), uses capillary assembly to organize PS spheres (~250 nm in diameter) into a close-packed lattice between glass slides.[96] Applying a brief heating at sub-T_g temperature (~110 °C, *i.e.*, 6 °C lower than the T_g) and ~5 MPa pressure eliminates voids while avoiding particle fusion. Cooling under the compressed state gives rise to a polyhedral lattice. The morphology of the polyhedral particles, *e.g.*, square, hexagonal, triangular, reflects their packing symmetry. The resulting polyhedral arrays display tunable optical diffraction that scales with particle size and compression. While this is a facile method to create polymeric polyhedra, it is limited to faceted morphologies. In addition, the particles near the boundaries deform differently from those in the bulk, leading to inherent heterogeneities. The separation and recovery of individual particles from the compressed lattice is likely non-trivial.

2.4. Microfluidic

Microfluidic devices enable the continuous production of shaped polymer microparticles by coupling droplet formation with rapid photopolymerization. Typically, a syringe pump drives the flow in a PDMS-molded channel (designed using

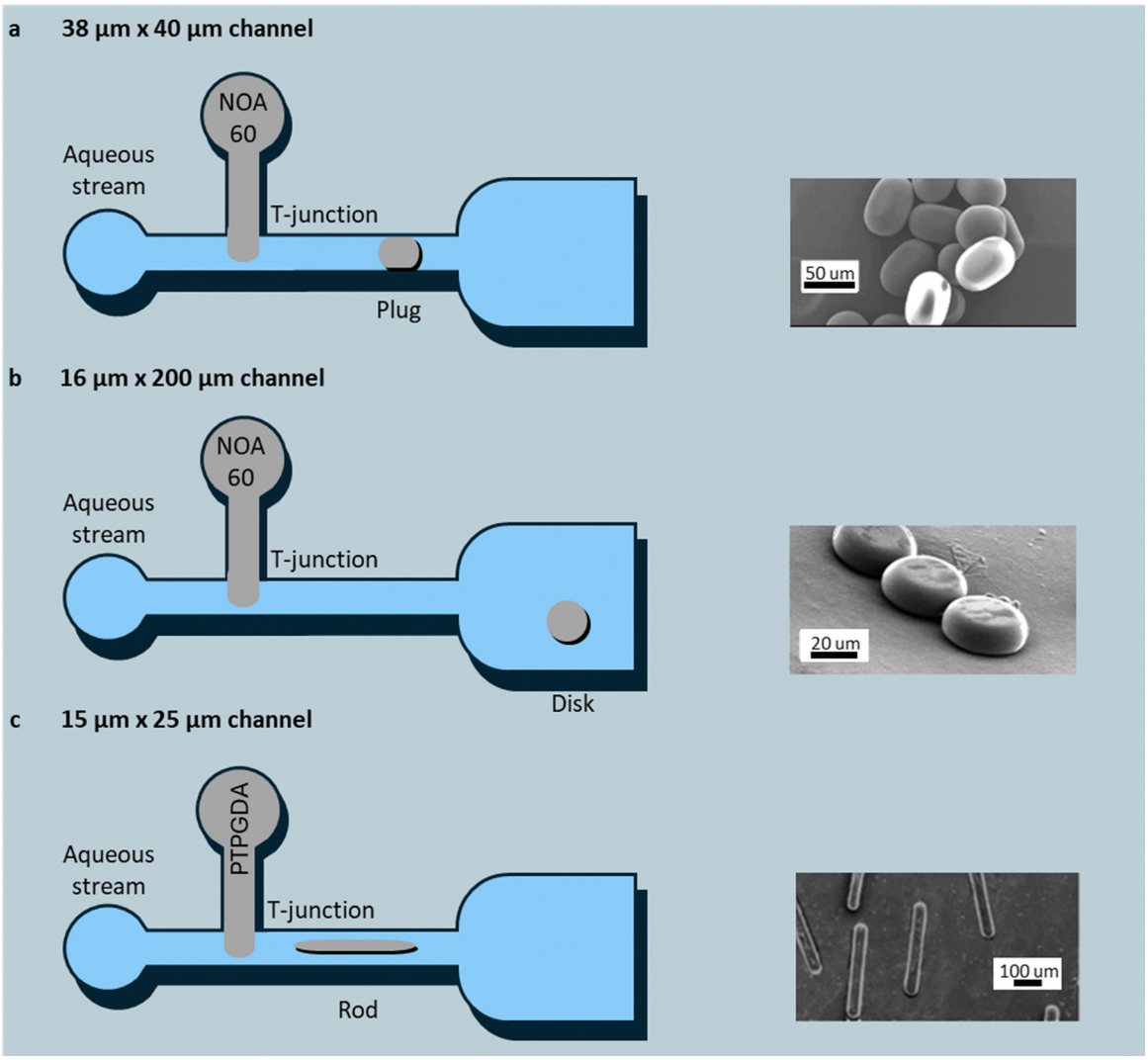

Fig. 8 Microfluidic channel-confinement schemes for the production of shaped particles, including (a) plug particles formed in a tall rectangular channel; (b) disk particles formed in a shallow channel. Reprinted from ref. 97 with permission from American Chemical Society, copyright 2005; (c) rod particles formed by forcing droplets through a constriction before UV curing. Reprinted from ref. 100 with permission from American Chemical Society, copyright 2005.

CAD and fabricated through lithography). The precursor solution (*i.e.*, monomer/polymer) can be emulsified in-line by mixing with an immiscible solvent (*e.g.*, water with small amounts of sodium dodecyl sulfate). Particle geometry is prescribed by (i) channel confinement (Fig. 8), (ii) interfacial tension in free droplets (Fig. 9), or (iii) patterned UV exposure of the flowing stream (Fig. 10). The Rayleigh–Plateau instability confines products to the 10–200 µm range, but the microfluidic devices deliver singly dispersed particles with deterministic control of their geometric dimensions. Simple channel designs yield plugs, rods, and disks; unconstrained coaxial droplets enable high-curvature ''hamburger'', ''olive'', and spherical-cap motifs; and mask projection produces virtually any planar extrusion.

2.4.1. Channel confinement. A UV-curable urethane-acrylate (*e.g.*, Norland Optical Adhesive 60, with a viscosity of 300 mPa s) has served as the dispersed phase and is pinched off by an aqueous SDS stream at a T-junction, producing singly dispersed droplets that adopt the channel cross-section before UV curing.[97–99] By introducing a photoinitiator, the polymer chemistry compatible with this method can be expanded to a variety of acrylates (TPGDA, EGDMA, and PETA-3/4).[100]

In 40 µm-wide, 38-µm high channels, droplets were shaped into plugs (Fig. 8a). A sub-microsecond UV flash then ''freezes'' the droplets into shaped particles. Reducing the channel height to 16 µm flattens the droplets into disks (Fig. 8b), whereas constrictions narrower than the droplet diameter stretch them into cylinders (Fig. 8c). Length and thickness of the particles follow directly from flow-rate ratios of 0.01 to 0.1 µL min^{-1}, as well as channel geometry, enabling deterministic tuning at throughputs up to 500 particles s^{-1} per chip.

While this method is straightforward to implement, the curing kinetics can introduce uncertainty. Insufficient initiator or UV exposure leads to a solid shell and liquid core, hence

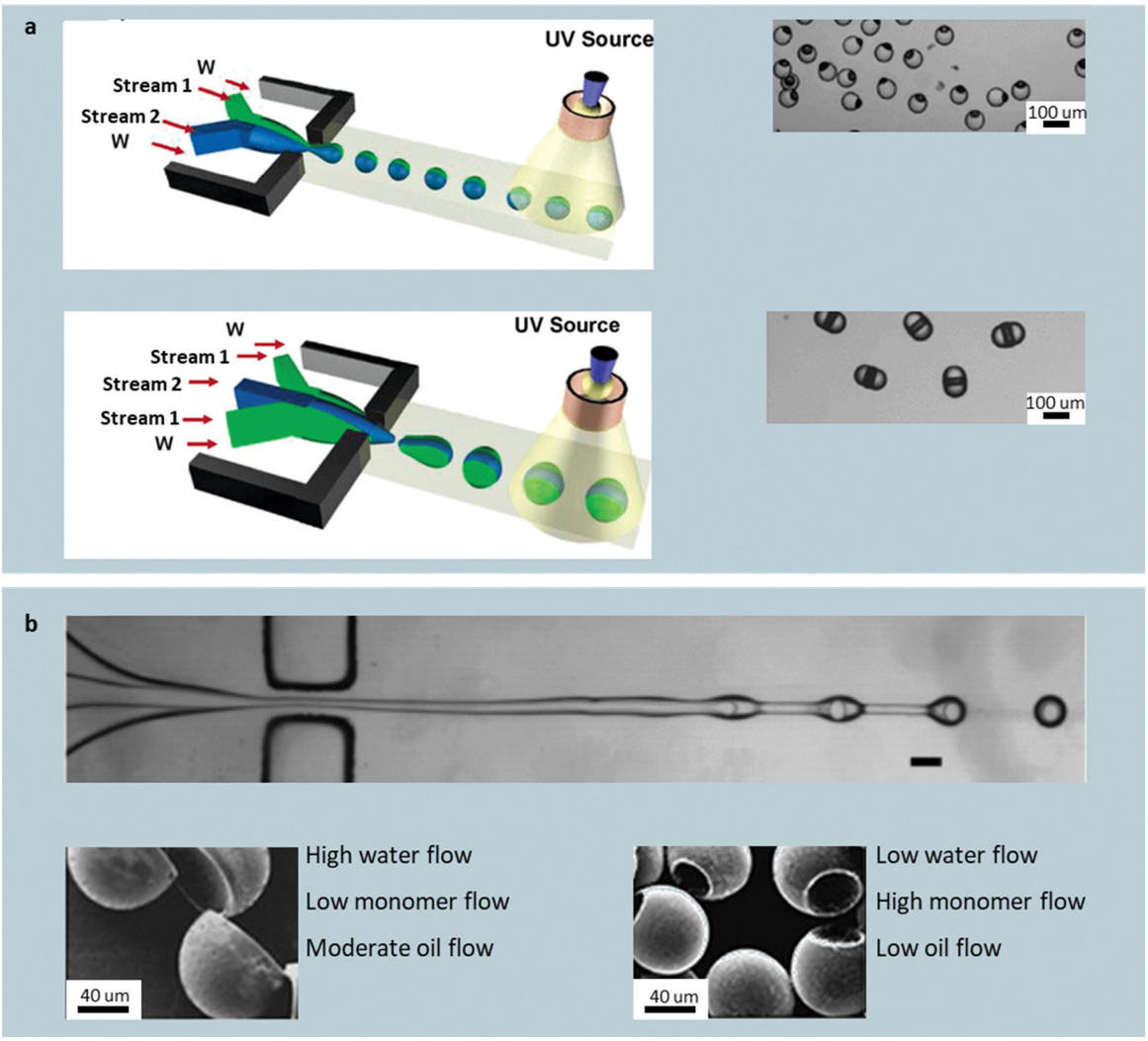

Fig. 9 Unconfined, interfacial-tension-guided particle shape engineering. (a) Olive particles from asymmetric coflow of two streams; hamburger particles from core–shell coflow. Reprinted from ref. 108 with permission from American Chemical Society, copyright 2006. Sacrificial-core comprising silicone oil for particles with concave compartments (b); concave spherical caps obtained at low water and high monomer flow rates; pitted olive particles at high water and low monomer and oil flow. Reprinted from ref. 109 with permission from American Chemical Society, copyright 2005.

buckling upon extraction, whereas rapid cures can 'burst' droplets into irregular blobs from the exothermic reaction. A narrow window of reaction conditions and pulse energy that has been optimized empirically is often required for the reliable production of defect-free particles.

2.4.2. Emulsified droplet without confinement. By avoiding the constraints of hard channels, particles with programmable curvature can be produced when the polymerizable and emulsified droplets experience shape evolution guided by interfacial tension and flow (Fig. 9a).[101–107] Two immiscible, photopolymerizable streams, *e.g.*, methacryloxypropyl dimethylsiloxane (stream 1) and PEGDA (45 wt%)/pentaerythritol triacrylate (45 wt%)/acrylic acid (5 wt%) blend (stream 2), have been co-sheathed in water/SDS for particles with discontinuous curvatures.[108] If one stream vastly outpaces the other in flow, it partially engulfs its neighbor upon pinching off and droplet formation; polymerization then yields ''olive'' particles with an embedded ''pit'' from the minor phase. Arranging the streams in a core–shell configuration and sheathing with water produces triple emulsions that solidify into ''hamburgers''.

Replacing stream 1 with sacrificial silicone oil introduces a concave compartment into the spherical particles (Fig. 9b). An example system comprises a coaxial jet, where a central stream of silicone oil (containing 0.2–2.0 wt% sorbitan monooleate or SPAN 80 to stabilize the oil–monomer interface during droplet formation) is wrapped by an acrylate stream (*e.g.*, tripropyleneglycol diacrylate or EGDMA) with 4 wt% of a photoinitiator (*e.g.*, 1-hydroxycyclohexyl phenyl ketone (HCPK)), which is sheathed in water with 2 wt% SDS.[109] Similarly to the previous method, the coaxial jet breaks into droplets due to Rayleigh–Plateau instability. Particles with a concave compartment can be achieved upon polymerization and oil extraction, with the morphology tunable *via* the flow rates of oil, monomer, or aqueous phase. Low water and high

monomer flow rates produce concave caps, whose aspect ratio decreases with the oil flow rate. High water and lower monomer and oil flows impose greater shear and smaller encapsulated volumes, shifting products to off-center, pitted-olive particles. These routes are continuous and produce singly dispersed particles, but are limited to concave geometries.

2.4.3. UV mask. Beyond droplet formation, microfluidic systems can sculpt polymer particles directly from a continuous flowing prepolymer stream, where patterned UV exposure defines the particle geometry.[110–114] In this approach, UV-curable prepolymer, typically 30–40 wt% PEGDA containing 1 wt% 2-hydroxy-2-methylpropiophenone photoinitiator in water, flows through a PDMS microchannel.[115] It is periodically exposed to UV light projected through a microscope objective and a photomask (Fig. 10a). The exposed regions undergo crosslinking, solidifying into particles whose in-plane dimensions correspond to the illuminated mask pattern, while the unexposed stream remains fluid and flushes the newly formed particles downstream. Using this stop-flow configuration, PEGDA prepolymer streams have been patterned into planar extrusions with invariant thickness in the *z*-direction, generating square (Fig. 10a(i)), hexagonal (Fig. 10a(ii)), circular (Fig. 10a(iii)), or triangular (Fig. 10a(iv)) particles. The particle size can be tuned by the optical magnification of the projection system, with higher magnifications yielding smaller features, but the cyclic stop-and-flow operation limits throughput and is prone to the risk of motion-induced distortion.

To overcome these constraints, a continuous-flow variant integrates the same photomask principle but exposes the moving prepolymer stream to rapid (<1 s) patterned UV flashes (Fig. 10b).[116] A PEGDA formulation, containing a commercially available photoinitiator, Darocur 1173 (an α-hydroxy-alkylphenone), continuously polymerizes into singly disperse rings (Fig. 10b(i)), triangles (Fig. 10b(ii)), cylinders (Fig. 10b(iii)), hexagons (Fig. 10b(iv)), cuboids (Fig. 10b(v)), flat lollipops (Fig. 10b(vi)), commas (Fig. 10b(vii)), and horseshoe-like particles (Fig. 10b(viii)). An AUTOCAD-designed photomask with $\sim$10 μm features is inserted at the microscope field stop, and the objective lens projects the pattern onto the flowing oligomer. A sub-second UV flash cures the illuminated cross-section, while oxygen diffusing through the PDMS channel prevents clogging by forming chain-terminating peroxide radicals near the channel surface (*via* a reaction with the initiator), leaving a thin unpolymerized lubrication layer. This continuous photolithographic microfluidic process achieves throughputs approaching 100 monodisperse particles s^{-1} per chip, while maintaining precise *xy*-plane fidelity. Although confined to planar extrusions and limited by optical depth of field, the UV-mask approach bridges conventional lithography and flow photopolymerization – offering mask-defined particle shapes without the need for molds or droplets.

2.5. Miscellaneous

A small class of unconventional fabrication methods broadens the shape palette of polymer particles by coupling polymer softening, vapor-phase condensation, or field-driven droplet shaping with straightforward bench-top setups. These approaches – often limited in throughput – demonstrate unique shape-forming mechanisms inaccessible to conventional lithography, emulsion, or microfluidic systems.

2.5.1. Vapor-based methods. Solvent-vapor relaxation reshapes preformed polymer spheres through vapor-induced softening and interfacial stress.[117–121] When ethanol–water-preswollen PS spheres (2 μm diameter) are introduced onto the surface of DI water within a sealed chamber containing a toluene reservoir, toluene vapor diffuses into the system and lowers the T_g of PS.[122] The resulting Marangoni stress at the air–liquid-particle interface spread the softened particles laterally, producing a sequential transformation from ridged Saturn-like structures (after 12 minutes) to UFO (16 minutes) and flattened disk-like particles (19–20 minutes) (Fig. 11a). Smaller spheres (*e.g.*, 610- and 240-nm diameter) deform faster because their higher surface-to-volume ratio facilitates vapor permeation. The process proceeds at room temperature and requires no external heat, but the method is restricted to solvent-compatible polymers and moderate batch sizes.

Replacing the water interface with a polymeric thin film expands the accessible morphologies. When PS spheres (10 μm) are spin-coated onto PMMA films and annealed in toluene vapor at 30 °C, swelling of both polymers enables wetting and partial sinking into the softened PMMA surface.[123] The sequence of shapes evolves predictably with annealing time, *i.e.*, bell (3 hours), UFO (4 hours), cymbal (6 hours), contact-lens (11 hours), and bowl (12 hours) geometries, reflecting progressive minimization of total surface and interfacial energies (Fig. 11b). To release the particles, PMMA can be dissolved using acetic acid. Contacting PS particles can fuse into various peanut-like shapes. Substituting toluene with cyclohexane, which swells PS but leaves PMMA rigid, halts the sinking behavior and produces uniformly flattened discs. The shape outcome can be tuned by solvent choice, vapor activity, and exposure duration, though the multi-hour processing limits throughput.

Polymer particles can also be synthesized directly from the vapor phase without any pre-existing seed. Condensed droplet polymerization (CDP) combines monomer condensation and radical-initiated polymerization under vacuum (1 mTorr–1 Torr).[124–128] Monomers with a double bond are vaporized and condensed as droplets onto a thermoelectrically cooled, non-wetting substrate (usually kept at $\leq$10 °C). A *tert*-butyl peroxide vapor feed is thermally decomposed by a heated filament array to generate radicals that initiate polymerization within the condensed droplets to form solid spherical domes. The droplet contact angle controls curvature; early-stage nucleation and condensation yield sub-100 nm domes, while later coalescence generates a bimodal, micrometer-scale population. The interplay between propagation rate constant (k_p) and T_g dictates the dome morphology: moderate k_p and T_g values yield smooth hemispherical domes, while high values produce wrinkled or fragmented shells after unreacted monomer removal (Fig. 11c). The dome particle size and distribution can be controlled in real time using optical and interferometric monitoring.

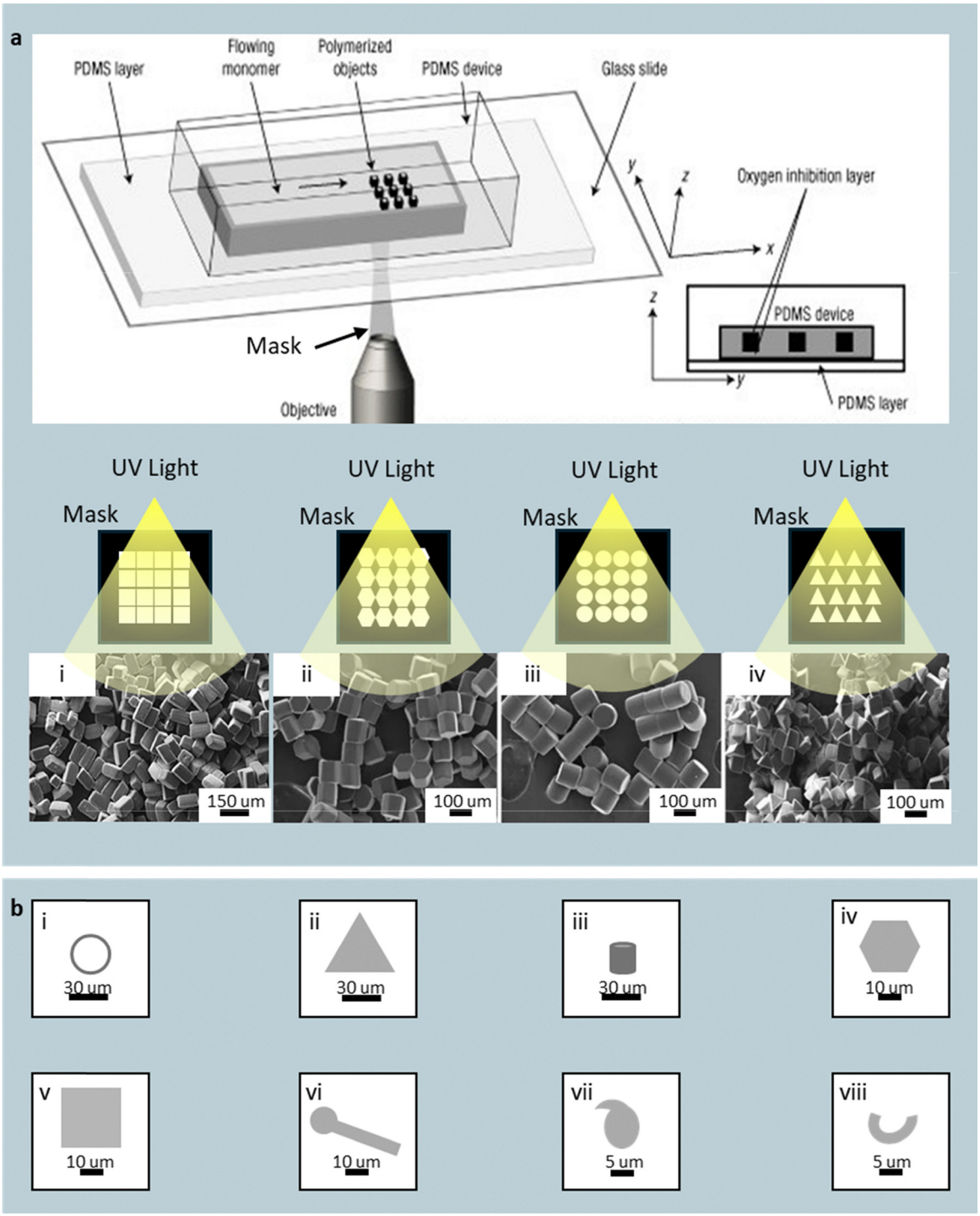

Fig. 10 UV-mask photopolymerization of flowing prepolymer streams in microfluidic channels. (a) Schematic showing a continuous stream of UV-curable prepolymer exposed to patterned UV light through a photomask, where the illuminated cross-sections polymerize into solid particles. Mask-defined shapes fabricated *via* stop-flow projection lithography include (a-i) square, (a-ii) hexagonal, (a-iii) circular, and (a-iv) triangular particles. Reprinted from ref. 115 with permission (open access) from Springer, copyright 2011. (b) Continuous-flow patterned UV exposure extends the accessible morphologies to (b-i) rings, (b-ii) triangles, (b-iii) cylinders, (b-iv) hexagons, (b-v) cuboids, (b-vi) flat lollipops, (b-vii) commas, and (b-viii) horseshoe-like particles. Oxygen diffusion through PDMS channel walls forms a thin inhibition layer that prevents wall adhesion and enables continuous downstream transport of the patterned particles.

CDP thus offers rapid (<1 min), solvent- and template-free fabrication of morphologically tunable particles, though its current product range remains limited to hemispherical and disc-like geometries. Nevertheless, a broad range of functional monomers—including hydrophilic, aromatic, amine-containing, and cross-linkable types—have been made into dome particles using CDP.

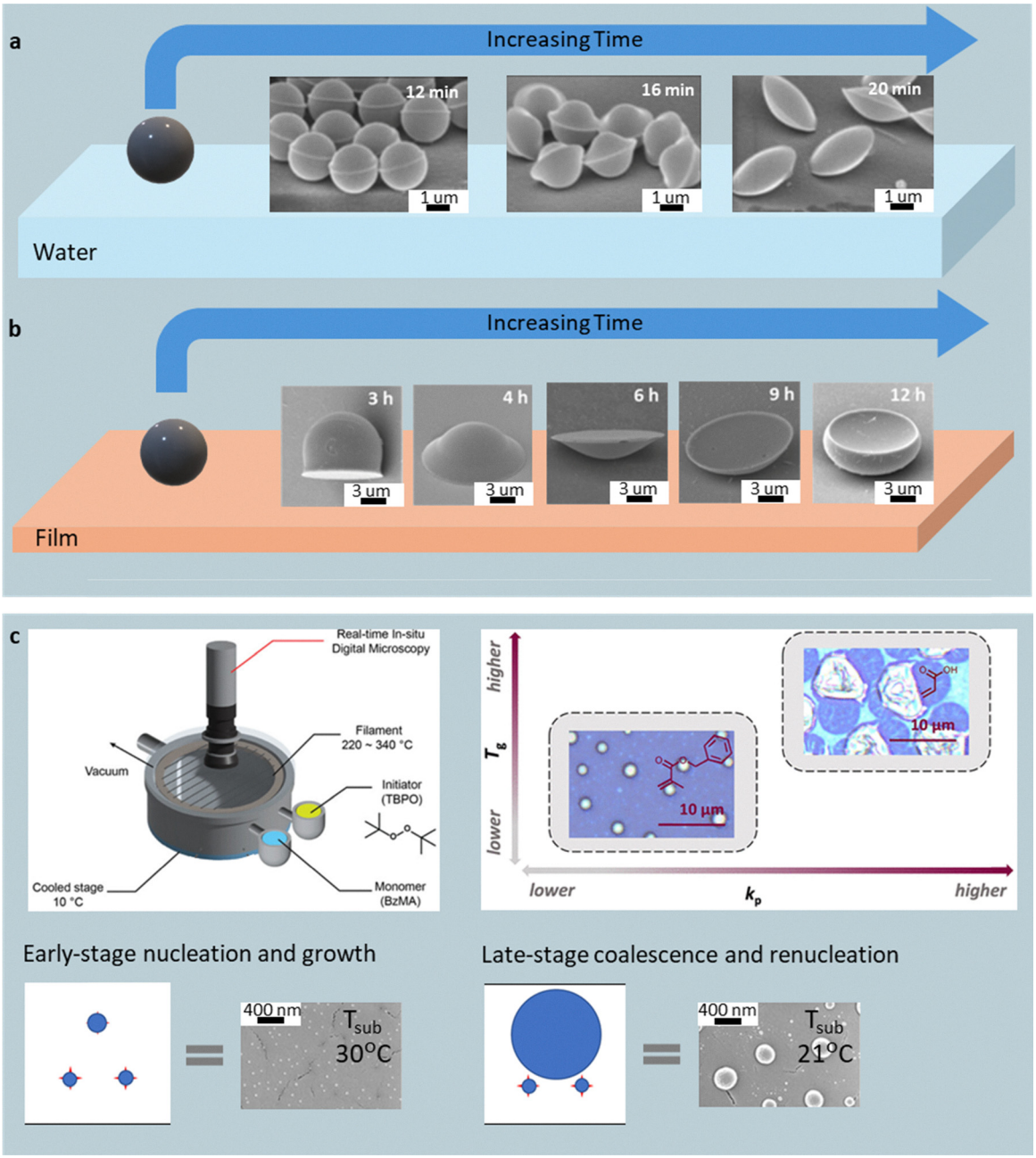

Fig. 11 Solvent-vapor and condensed-droplet shaping of polymer particles. (a) Particle-on-water method in the presence of the vapor of an organic solvent relaxes PS spheres to form Saturn-, UFO-, and disk-shaped particles. Reprinted from ref. 122 with permission from Wiley, copyright 2016. (b) Particle-on-film in the presence of the vapor of an organic solvent produces bell, UFO, cymbal, contact lens, and bowl geometries. Reprinted from ref. 123 with permission from American Chemical Society, copyright 2017. (c) Schematic of CDP (Reprinted from ref. 127 with permission from Wiley, copyright 2025), combining vapor condensation and radical polymerization (Reprinted from ref. 126 with permission from American Chemical Society, copyright 2023) to yield a unimodal distribution of nanodomes or a bimodal distribution of larger synthesized microdomes. Reprinted from ref. 125 with permission from Thieme, copyright 2023.

2.5.2. Electrospraying. Electrospraying shapes polymer particles through electrohydrodynamic breakup.[129,130] When a high voltage is applied to a polymer solution emerging from a fine needle, the liquid forms a Taylor cone and ejects charged droplets. The droplet trajectory is guided by the electric field. They solidify either during flight or upon contacting a substrate or a crosslinking bath. The interplay among jet voltage, solution composition, flight distance, and the solidification rate governs the resulting geometry.

In one representative setup, a 2 wt% alginate solution is electrosprayed through a 50 μm needle toward a calcium–chloride ($CaCl_2$) crosslinking bath (Fig. 12a).[131] The distance between the syringe and bath sets the droplet flight time, while $CaCl_2$ concentration dictates the gelation rate. Short distances

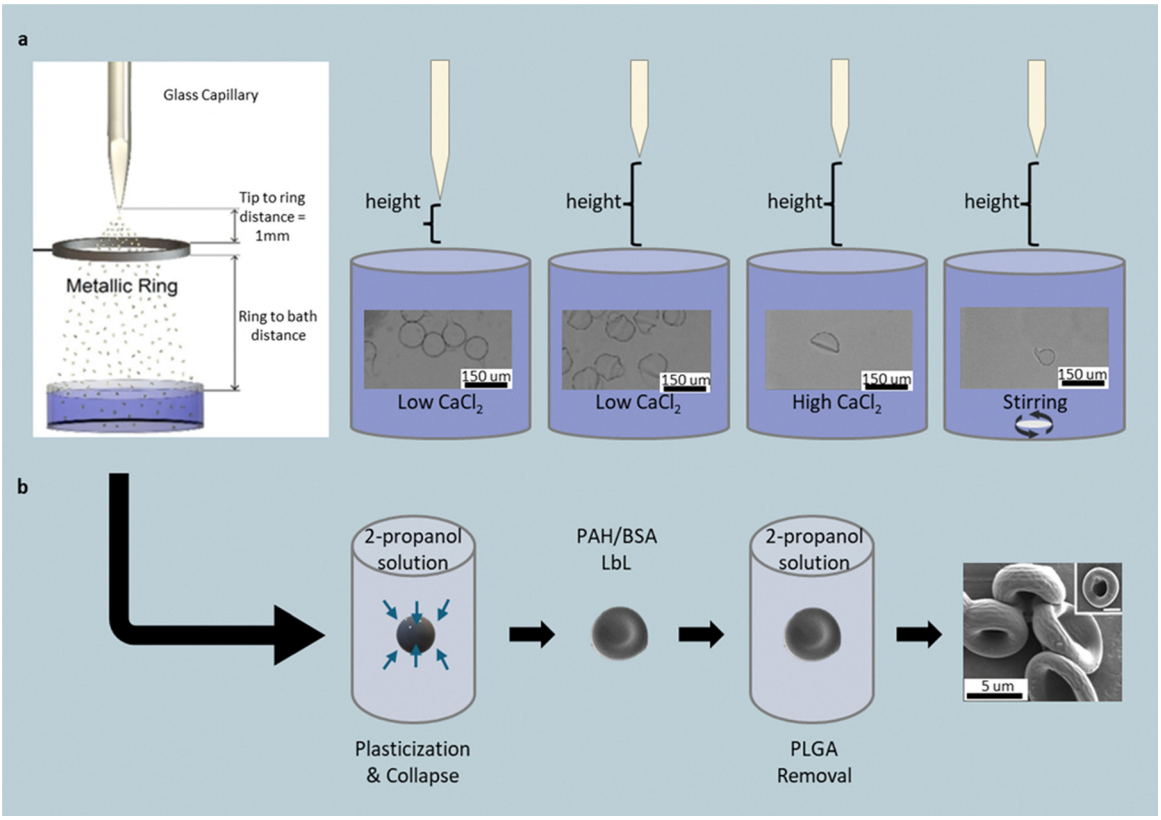

Fig. 12 Electrospraying and electrohydrodynamic jetting to shape polymer particles. (a) Schematic of the electrospraying setup in which 2 wt% alginate droplets are crosslinked by $CaCl_2$ to form acorn-, gumdrop-, and hemisphere-like particles. Stirring the crosslinking bath yields comma-shaped particles. Reprinted from ref. 131 with permission from Wiley, copyright 2018. (b) Hollow, red-blood-cell-like protein capsules generated from solvent-plasticized PLGA templates coated *via* layer-by-layer deposition and core removal. Reprinted from ref. 132 with permission from National Academy of Sciences, USA, copyright 2009.

(3 mm) and low $CaCl_2$ concentrations (1–2.5 wt%) yield tailed spherical particles, while longer distances (20 mm) promote gumdrop geometries, and high $CaCl_2$ concentrations (7.5–10 wt%) rapidly fix hemispherical shapes upon impact, preserving the flattened base. Introducing shear to the bath (*e.g.*, stirring at 50–500 rpm) elongates droplets into teardrop or comma-shaped particles as they gel. This method operates at room temperature, produces hundreds of microparticles per second, though particle sizes typically remain in the 100–300 μm range and are confined to hydrogel chemistries.

Electrospray principles can also be extended to solvent-driven deformation of solid polymer spheres. PLGA particles produced by electrohydrodynamic jetting are briefly immersed in 2-propanol to plasticize their outer shells, which buckle under internal stress to form biconcave discs.[132] Subsequent layer-by-layer deposition of poly(allylamine hydrochloride) and bovine serum albumin, followed by PLGA dissolution, leaves hollow red-blood-cell-like protein capsules. Analogous structures can be fabricated from commercial hollow polystyrene beads by applying the same coating process and dissolving the core in tetrahydrofuran (Fig. 12b). These solvent-triggered plasticization routes enable reproducible formation of concave, biomimetic particles, though they rely on organic solvents and post-processing steps that limit scalability.

3. Discussion and conclusion

The diversity of accessible polymer particle morphologies, from rods and discs to bowls, lobes, and polyhedral, reflects a unified set of governing principles across fabrication families. Shape evolution is dictated by four dominant parameters: (i) geometric confinement (molds, microchannels, or colloidal packings), (ii) interfacial tension and wetting contrasts that prescribe curvature, (iii) polymer chain mobility relative to the reaction or deformation rate ($T-T_g$), and (iv) external field gradients (mechanical strain, shear, or electric fields). Together, these parameters define the thermodynamic and kinetic envelope that fixes particle geometry during chemical or physical solidification.

Each method family occupies a distinct mechanistic and operational niche. Lithography and template molding deliver precise *xy*-plane fidelity for prismatic or extruded shapes, yet scale poorly. Seeded emulsion polymerization achieves diverse lobed or Janus morphologies *via* phase separation but depends strongly on polymer compatibility. Mechanical deformation reshapes spherical feedstock into rods, discs, or polyhedra using simple protocols but suffers from strain heterogeneity. Microfluidic photopolymerization produces monodisperse extruded or high-curvature particles but requires chip parallelization for scale-up. Vapor-based processes and CDP yield

flattened or hemispherical shapes with minimal solvent use but require specialty reactors, while electrospraying converts the field force into shape anisotropy across hydrogel or thermoplastic systems.

Across methods, the attainable particle size is ultimately set by the specific length-scale bottleneck that creates and then preserves anisotropy. Templated lithography/imprint is constrained by mask or mold feature size and by release/harvest fidelity; mask-defined photolithography readily targets micron-scale features. At the same time, nanomolding can push to sub-100-nm features but is limited by rounding and feature fidelity at the smallest dimensions.[22,36] Microfluidic methods are constrained by channel geometry and the droplet/confinement regimes that remain monodisperse, as particle dimensions track the channel width/height and the breakup windows, rather than being freely selectable.[95,98,107] Seeded growth/seeded emulsion routes are constrained by the seed size and by swelling/monomer transport through (and compatibility with) the seed network; sufficiently small or highly constrained seeds can suppress the phase separation needed for anisotropy, and practical diffusion/annealing windows bound what is realizable.[38,43,55,57] By contrast, mechanical deformation/reshaping is constrained by T_g-dependent chain mobility and strain homogeneity, as the shape-setting step requires softening above T_g or solvent plasticization and is additionally bounded by the available starting sphere sizes and handling/recovery limits.[79,87,92] Accordingly, the demonstrated size windows and their limiting mechanisms are best interpreted together (and are tabulated as such) rather than treated as independent descriptors.[22,36,38,79,95]

At larger production scales, the dominant constraint is usually how effectively a method can be parallelized and how robustly particles can be harvested/collected, not simply the curing/polymerization chemistry. In templated approaches (lithography, imprinting, and related mold-replication), output scales most directly with patterned area (mask/mold/wafer size) and cycle repetition (fill-cure-release).[25,32,36] Roll-to-roll mold templating (*e.g.*, PRINT-style micromolding) may be well-positioned for scale-up because it replaces "one exposure at a time" with continuous cavity filling and repeated harvesting.[29,35] Flow-based platforms are continuous, but the output is typically limited by device multiplexing (number of channels/emitters or illumination lanes) and downstream handling.[98,101,103,107] Similar issues exist for continuous-flow and stop-flow lithographic platforms. Nevertheless, a productivity of multi-million particles per hour in multi-channel implementations has been reported.[108,114] In summary, methods that are easiest to parallelize in hardware and easiest to harvest cleanly may be the most promising candidates for large-scale production.[25,29,32,36,101,107,108]

Future advancements hinge on four imperatives: standardization, sustainability, scalability, and use-inspired demonstration of emergent properties for the shaped particles. Reporting shape yield, throughput normalized by device area or polymer mass, and energy or solvent consumption will enable direct comparison between methods. Sustainable chemistries, from solvent-free polymerization to recyclable elastomers, and to PFAS-free molds, will improve process viability and scalability. Semi-continuous processes such as roll-to-roll PRINT or chemical vapor deposition hint that shape-engineered polymer particles are approaching market readiness. *In situ*, AI-supervised synthesis could soon automate parameter selection and deliver on-demand geometries. Finally, translating these shape libraries into real-world testing will reveal where geometry delivers tangible performance gains. For example, ellipsoid and discoidal are often favored in circulation and cellular uptake studies, due to their margination under flow (to prolong circulation time) and differential clearance times by specific immune cells.[133,134] Hemispherical, concave, or convex shapes resemble optical lenses and can enable future optical metamaterials.[127] The shapes of Janus and lobed/clustered particles can be leveraged to direct self-assembly, giving rise to emergent properties like superhydrophobicity or modulated reflectivity.[135,136] Polyhedral and prismatic particles may assemble into materials with programmable photonic band gaps.[137] While concave forms like bowls can enclose and/or transport cargo, extruded shapes like rods, plugs, or filaments have served as building blocks for higher-order assembly or interlocking interfaces for targeted combinations of mechanical, interfacial, and bulk properties.[138,139] The future of shape-engineered polymer particles lies in their ability to be implemented in real-world applications. For example, tissue repair constructs that utilize particle-laden hydrogels may benefit from the anisotropic packing of rod particles for greater integration and faster tissue regeneration.[140]

In the near term, commercial adoption will likely favor single-shape, high-yield systems. Hybrid workflows that merge complementary mechanisms, *e.g.*, microfluidic pre-shaping followed by vapor relaxation, could offer both precision and scalability. Ultimately, geometry will join chemistry and size as a core design variable in polymer particle engineering, reshaping the material logic of applications spanning healthcare, consumer goods, and structural composites.

Author contributions

JDJ conducted the literature search. EL and JDJ created the figures. JDJ and RY composed and revised the manuscript. RY directed the study.

Conflicts of interest

R. Y. holds equity in Oto Biotech. EL and JDJ have no conflicts to declare.

Data availability

No primary research results, software, or code have been included, and no new data were generated or analyzed as part of this review.

Acknowledgements

This work was supported in part by the National Science Foundation Faculty Early Career Development Program [grant number CMMI-2144171]. J. J. is supported by the NSF Graduate Research Fellowship Program (GRFP) under Grant No. DGE-2139899 and the Cornell Engineering Lance R. Collins Fellowship. E. L. is supported by the Cornell Engineering Learning Initiatives Undergraduate Research Fund.

References

1 American Chemical Society National Historic Chemical Landmarks. U.S. Synthetic Rubber Program.
2 D. Foord, *Enterp. Soc.*, 2023, **24**, 395–424.
3 M. Antonietti and K. Tauer, *Macromol. Chem. Phys.*, 2003, **204**, 207–219.
4 P. A. Lovell and F. J. Schork, *Biomacromolecules*, 2020, **21**, 4396–4441.
5 D. N. Petsev, N. D. Denkov and P. A. Kralchevsky, *J. Colloid Interface Sci.*, 1995, **176**, 201–213.
6 P. Ahlin Grabnar and J. Kristl, *J. Microencapsul.*, 2011, **28**, 323–335.
7 A. D. Bangham, M. M. Standish and J. C. Watkins, *J. Mol. Biol.*, 1965, **13**, 238-IN27.
8 K. K. Jain, in *Drug Delivery Systems*, ed K. K. Jain, Springer New York, New York, NY, 2020, vol. 2059, pp. 1–54.
9 A. Sultana, M. Zare, V. Thomas, T. S. S. Kumar and S. Ramakrishna, *Med. Drug Discovery*, 2022, **15**, 100134.
10 S. Senapati, A. K. Mahanta, S. Kumar and P. Maiti, *Signal Transduction Targeted Ther.*, 2018, **3**, 7.
11 N. Deirram, C. Zhang, S. S. Kermaniyan, A. P. R. Johnston and G. K. Such, *Macromol. Rapid Commun.*, 2019, **40**, 1800917.
12 S. R. Sershen, S. L. Westcott, N. J. Halas and J. L. West, *J. Biomed. Mater. Res.*, 2000, **51**, 293–298.
13 A. Chilkoti, M. R. Dreher, D. E. Meyer and D. Raucher, *Adv. Drug Delivery Rev.*, 2002, **54**, 613–630.
14 O. Pillai and R. Panchagnula, *Curr. Opin. Chem. Biol.*, 2001, **5**, 447–451.
15 P. J. Gawne, M. Ferreira, M. Papaluca, J. Grimm and P. Decuzzi, *Nat. Rev. Mater.*, 2023, **8**, 783–798.
16 V. Kozlovskaya, M. Dolmat and E. Kharlampieva, *ACS Appl. Polym. Mater.*, 2021, **3**, 2274–2289.
17 H. Hadji and K. Bouchemal, *J. Controlled Release*, 2022, **342**, 93–110.
18 N. Kapate, J. R. Clegg and S. Mitragotri, *Adv. Drug Delivery Rev.*, 2021, **177**, 113807.
19 P. Li, J. Zhang, X. Liu, X. Zhang, J. Ma, G. Sun, L. Hou and S. Raza, *Polym. Chem.*, 2025, **16**, 774–799.
20 D. Jiang, S. Liu and W. Tang, *Micromachines*, 2022, **13**, 1659.
21 P. Lagarrigue, F. Moncalvo and F. Cellesi, *Pharmaceutics*, 2022, **15**, 32.
22 R. K. Pal, N. E. Kurland, C. Jiang, S. C. Kundu, N. Zhang and V. K. Yadavalli, *Eur. Polym. J.*, 2016, **85**, 421–430.
23 B. Li, M. He, L. Ramirez, J. George and J. Wang, *ACS Appl. Mater. Interfaces*, 2016, **8**, 4158–4164.
24 C. Lu and R. H. Lipson, *Laser Photonics Rev.*, 2010, **4**, 568–580.
25 J.-H. Jang, C. K. Ullal, S. E. Kooi, C. Koh and E. L. Thomas, *Nano Lett.*, 2007, **7**, 647–651.
26 L. E. Roode, H. Brighton, T. Bo, J. L. Perry, M. C. Parrott, F. Kersey, J. C. Luft, J. E. Bear, J. M. DeSimone and I. J. Davis, *Nanomed. Nanotechnol. Biol. Med.*, 2016, **12**, 1053–1062.
27 D. A. Canelas, K. P. Herlihy and J. M. DeSimone, *Wiley Interdiscip. Rev.: Nanomed. Nanobiotechnol.*, 2009, **1**, 391–404.
28 K. B. Wiles, N. S. Wiles, K. P. Herlihy, B. W. Maynor, J. P. Rolland and J. M. DeSimone, in *Soft lithography using perfluorinated polyether molds and PRINT technology for fabrication of 3-D arrays on glass substrates*, ed M. J. Lercel, San Jose, CA, 2006, p. 61513F.
29 A. Garcia, P. Mack, S. Williams, C. Fromen, T. Shen, J. Tully, J. Pillai, P. Kuehl, M. Napier, J. M. DeSimone and B. W. Maynor, *J. Drug Delivery*, 2012, **2012**, 1–10.
30 S. E. A. Gratton, P. D. Pohlhaus, J. Lee, J. Guo, M. J. Cho and J. M. DeSimone, *J. Controlled Release*, 2007, **121**, 10–18.
31 V. Kudryavtseva, A. Bukatin, E. Vyacheslavova, D. Gould and G. B. Sukhorukov, *Biomater. Adv.*, 2022, **136**, 212762.
32 F. Buyukserin, M. Aryal, J. Gao and W. Hu, *Small*, 2009, **5**, 1632–1636.
33 B. Xue, V. Kozlovskaya and E. Kharlampieva, *J. Mater. Chem. B*, 2017, **5**, 9–35.
34 N. Higuita-Castro, D. Gallego-Perez, K. Love, M. R. Sands, G. Kaletunç and D. J. Hansford, *Ind. Biotechnol.*, 2012, **8**, 365–371.
35 Y. Wang, Y. Wang, X. Zheng, G.-R. Yi, S. Sacanna, D. J. Pine and M. Weck, *J. Am. Chem. Soc.*, 2014, **136**, 6866–6869.
36 F. Caruso, R. A. Caruso and H. Möhwald, *Science*, 1998, **282**, 1111–1114.
37 J. L. Perry, K. P. Herlihy, M. E. Napier and J. M. DeSimone, *Acc. Chem. Res.*, 2011, **44**, 990–998.
38 L. C. Glangchai, M. Caldorera-Moore, L. Shi and K. Roy, *J. Controlled Release*, 2008, **125**, 263–272.
39 G. Zhou, S. Liu, W. Liu, D. Yuan and G. Zhou, *Micromachines*, 2019, **10**, 441.
40 J.-W. Kim and K.-D. Suh, *J. Ind. Eng. Chem.*, 2008, **14**, 1–9.
41 N. Sudjaipraparat, C. Kaewsaneha, S. Nuasaen and P. Tangboriboonrat, *Polymer*, 2017, **121**, 165–172.
42 X. Pei, K. Zhai, X. Liang, Y. Deng, K. Xu, Y. Tan, X. Yao and P. Wang, *J. Colloid Interface Sci.*, 2018, **512**, 600–608.
43 M. Yang, Y. Guo, Q. Wu, Y. Luan and G. Wang, *Polymer*, 2014, **55**, 1948–1954.
44 Y.-S. Cho, S.-H. Kim and J. H. Moon, *Korean J. Chem. Eng.*, 2012, **29**, 1102–1107.
45 H. R. Sheu, M. S. El-Aasser and J. W. Vanderhoff, *J. Polym. Sci., Part A: Polym. Chem.*, 1990, **28**, 653–667.
46 C. Wei, A. Plucinski, S. Nuasaen, A. Tripathi, P. Tangboriboonrat and K. Tauer, *Macromolecules*, 2017, **50**, 349–363.
47 S. Wang, Y. Long, H. Liu and F. Liang, *Macromolecules*, 2025, **58**, 5927–5936.
48 S. Jia, H. Wang, R. Tang, S. Ma, B. Gong and J. Ou, *Polymer*, 2023, **265**, 125604.
49 B. Peng, H. R. Vutukuri, A. Van Blaaderen and A. Imhof, *J. Mater. Chem.*, 2012, **22**, 21893.
50 X. Meng and D. Qiu, *Polymer*, 2020, **203**, 122799.
51 S. Wang and N. Wu, *Langmuir*, 2015, **31**, 7962–7969.
52 E. Y. K. Fung, K. Muangnapoh and C. M. Liddell Watson, *J. Mater. Chem.*, 2012, **22**, 10507.
53 B. Peng and A. Imhof, *Soft Matter*, 2015, **11**, 3589–3598.
54 B. Peng, A. Van Blaaderen and A. Imhof, *ACS Appl. Mater. Interfaces*, 2013, **5**, 4277–4284.
55 Y. Li, F. Liu, S. Demirci, U. K. Dey, T. Rawah, A. Chaudary, R. Ortega, Z. Yang, E. Pirhadi, B. Huang, X. Yong and S. Jiang, *Nanoscale*, 2025, **17**, 88–112.
56 F. Wang, H. Liu, L. Zhao and X. Zhang, *Colloid Polym. Sci.*, 2014, **292**, 1171–1179.
57 Y.-C. Lin, A. K. Tripathi and J. G. Tsavalas, *ACS Appl. Polym. Mater.*, 2022, **4**, 313–326.
58 L. Tian, X. Li, P. Zhao, Z. Ali and Q. Zhang, *Macromolecules*, 2016, **49**, 9626–9636.
59 G. Russo and M. Lattuada, *J. Colloid Interface Sci.*, 2022, **611**, 377–389.
60 Y. Saadat, S. Hosseinzadeh, S. Abdolbaghi and F. Afshar-Taromi, *Colloid Polym. Sci.*, 2013, **291**, 1113–1120.
61 J.-W. Kim, R. J. Larsen and D. A. Weitz, *Adv. Mater.*, 2007, **19**, 2005–2009.
62 S. Hosseinzadeh and Y. Saadat, *RSC Adv.*, 2015, **5**, 35325–35337.
63 Y. Saadat, S. Hosseinzadeh, F. Afshar-Taromi and H. Eslami, *Colloid Polym. Sci.*, 2012, **290**, 1099–1106.
64 J.-B. Fan, H. Liu, Y. Song, Z. Luo, Z. Lu and S. Wang, *Macromolecules*, 2018, **51**, 1591–1597.
65 N. Konishi, T. Fujibayashi, T. Tanaka, H. Minami and M. Okubo, *Polym. J.*, 2010, **42**, 66–71.
66 H. Zou, D. Miao, H. Sun and X. Wang, *Langmuir*, 2018, **34**, 14302–14308.
67 H. Zou, D. Miao, H. Sun and X. Wang, *Langmuir*, 2018, **34**, 14302–14308.
68 Y. Sun, F. Liang, X. Qu, Q. Wang and Z. Yang, *Macromolecules*, 2015, **48**, 2715–2722.
69 C. Li, Y. Yu, L. Wang, S. Zhang, J. Liu, J. Zhang, A.-B. Xu, Z. Wu, J. Tong, S. Wang, M. Xiao, Y. Fang, J. Yao, A. A. Solovev, B. Dong and L. He, *Chem. Mater.*, 2019, **31**, 9513–9521.

70 S. Sacanna, W. T. M. Irvine, P. M. Chaikin and D. J. Pine, *Nature*, 2010, **464**, 575–578.
71 Y. Wang, Y. Wang, X. Zheng, G.-R. Yi, S. Sacanna, D. J. Pine and M. Weck, *J. Am. Chem. Soc.*, 2014, **136**, 6866–6869.
72 H. Adelnia, J. N. Gavgani and M. Soheilmoghaddam, *Colloid Polym. Sci.*, 2015, **293**, 2445–2450.
73 X. Xie, Z. Ling, D. Li and H. Zou, *Langmuir*, 2025, **41**, 19914–19923.
74 J. Liao, C. Zhu, Z. He, J. Zhang, Y. Zeng and Z. Gu, *Langmuir*, 2022, **38**, 12132–12139.
75 Y. Jiang, L. Zhao, R. Li and H. Zou, *Langmuir*, 2024, **40**, 25811–25821.
76 W.-H. Chen, F. Tu, L. C. Bradley and D. Lee, *Chem. Mater.*, 2017, **29**, 2685–2688.
77 A. Namjoo, S. Abdolbaghi, Y. Saadat and S. Hosseinzadeh, *Colloid Polym. Sci.*, 2015, **293**, 1781–1789.
78 N.-H. Park, S.-I. Park and K.-D. Suh, *Colloid Polym. Sci.*, 2001, **279**, 1082–1089.
79 Z. Gong, T. Hueckel, G.-R. Yi and S. Sacanna, *Nature*, 2017, **550**, 234–238.
80 Y. Wang, J. T. McGinley and J. C. Crocker, *Langmuir*, 2017, **33**, 3080–3087.
81 E. Ben-Akiva, K. R. Rhodes, R. A. Meyer and J. J. Green, *J. Vis. Exp.*, 2018, 58332.
82 M. J. Heslinga, E. M. Mastria and O. Eniola-Adefeso, *J. Controlled Release*, 2009, **138**, 235–242.
83 W. Li, T. Suzuki and H. Minami, *Angew. Chem., Int. Ed.*, 2018, **57**, 9936–9940.
84 M. K. Klein, N. R. Saenger, S. Schuetter, P. Pfleiderer and A. Zumbusch, *Langmuir*, 2014, **30**, 12457–12464.
85 W. Tuntanatewin, P. Mekwatanakarn, H. Zhang and Y. Okamura, *J. Appl. Polym. Sci.*, 2021, **138**, 49798.
86 A. R. Bhide and A. B. Jindal, *Int. J. Pharm.*, 2021, **605**, 120820.
87 Q. Guo, C. J. Bishop, R. A. Meyer, D. R. Wilson, L. Olasov, D. E. Schlesinger, P. T. Mather, J. B. Spicer, J. H. Elisseeff and J. J. Green, *ACS Appl. Mater. Interfaces*, 2018, **10**, 13333–13341.
88 F. Zhang, T. Zhao, D. Ruiz-Molina, Y. Liu, C. Roscini, J. Leng and S. K. Smoukov, *ACS Appl. Mater. Interfaces*, 2020, **12**, 47059–47064.
89 J. A. Champion, Y. K. Katare and S. Mitragotri, *Proc. Natl. Acad. Sci. U. S. A.*, 2007, **104**, 11901–11904.
90 R. A. Meyer, R. S. Meyer and J. J. Green, *J. Biomed. Mater. Res. A*, 2015, **103**, 2747–2757.
91 Y. Hu, J. Ge, T. Zhang and Y. Yin, *Adv. Mater.*, 2008, **20**, 4599–4602.
92 C. Palazzo, G. Ponchel, J. J. Vachon, S. Villebrun, F. Agnely and C. Vauthier, *Int. J. Polym. Mater. Polym. Biomater.*, 2017, **66**, 416–424.
93 S. J. Ahn, K. H. Ahn and S. J. Lee, *Colloid Polym. Sci.*, 2016, **294**, 859–867.
94 H. Zhang, W. Tuntanatewin, K. Ishikura, D. Sogabe, K. Sugawara, A. Tokui, A. Nakagawa and Y. Okamura, *ACS Appl. Polym. Mater.*, 2020, **2**, 3355–3364.
95 H. Minami, A. Kojima and T. Suzuki, *Langmuir*, 2017, **33**, 1541–1546.
96 Z. Q. Sun, X. Chen, J. H. Zhang, Z. M. Chen, K. Zhang, X. Yan, Y. F. Wang, W. Z. Yu and B. Yang, *Langmuir*, 2005, **21**, 8987–8991.
97 D. Dendukuri, K. Tsoi, T. A. Hatton and P. S. Doyle, *Langmuir*, 2005, **21**, 2113–2116.
98 J. Kim and S. A. Vanapalli, *Langmuir*, 2013, **29**, 12307–12316.
99 I. Kobayashi, M. A. Neves, T. Yokota, K. Uemura and M. Nakajima, *Ind. Eng. Chem. Res.*, 2009, **48**, 8848–8855.
100 M. Seo, Z. Nie, S. Xu, M. Mok, P. C. Lewis, R. Graham and E. Kumacheva, *Langmuir*, 2005, **21**, 11614–11622.
101 S.-H. Kim, A. Abbaspourrad and D. A. Weitz, *J. Am. Chem. Soc.*, 2011, **133**, 5516–5524.
102 C.-H. Chen, R. K. Shah, A. R. Abate and D. A. Weitz, *Langmuir*, 2009, **25**, 4320–4323.
103 T. Nisisako and T. Torii, *Adv. Mater.*, 2007, **19**, 1489–1493.
104 H.-Y. Yang, M.-J. Zhang, X.-H. Guo, Y. Deng, P. Zhang, L.-D. Qiu, W. Wang and L.-Y. Chu, *Langmuir*, 2025, **41**, 30621–30632.
105 T. Nisisako and T. Hatsuzawa, *Microfluid. Nanofluidics*, 2010, **9**, 427–437.
106 D. C. Pregibon, M. Toner and P. S. Doyle, *Science*, 2007, **315**, 1393–1396.
107 K. Feng, N. Gao, W. Zhang, K. Zhou, H. Dong, P. Wang, L. Tian, G. He and G. Li, *Small*, 2020, **16**, 1903884.
108 Z. Nie, W. Li, M. Seo, S. Xu and E. Kumacheva, *J. Am. Chem. Soc.*, 2006, **128**, 9408–9412.
109 Z. Nie, S. Xu, M. Seo, P. C. Lewis and E. Kumacheva, *J. Am. Chem. Soc.*, 2005, **127**, 8058–8063.
110 G. C. Le Goff, J. Lee, A. Gupta, W. A. Hill and P. S. Doyle, *Adv. Sci.*, 2015, **2**, 1500149.
111 M. Li, D. Joung, J. A. Kozinski and D. K. Hwang, *Langmuir*, 2017, **33**, 184–190.
112 D. Dendukuri, T. A. Hatton and P. S. Doyle, *Langmuir*, 2007, **23**, 4669–4674.
113 S. K. Suh, K. Yuet, D. K. Hwang, K. W. Bong, P. S. Doyle and T. A. Hatton, *J. Am. Chem. Soc.*, 2012, **134**, 7337–7343.
114 D. K. Hwang, J. Oakey, M. Toner, J. A. Arthur, K. S. Anseth, S. Lee, A. Zeiger, K. J. Van Vliet and P. S. Doyle, *J. Am. Chem. Soc.*, 2009, **131**, 4499–4504.
115 D. Baah, J. Tigner, K. Bean, N. Walker, B. Britton and T. Floyd-Smith, *Microfluid. Nanofluid.*, 2012, **12**, 657–662.
116 D. Dendukuri, D. C. Pregibon, J. Collins, T. A. Hatton and P. S. Doyle, *Nat. Mater.*, 2006, **5**, 365–369.
117 B. J. Park and E. M. Furst, *Langmuir*, 2010, **26**, 10406–10410.
118 M. Sabapathy, Y. Shelke, M. G. Basavaraj and E. Mani, *Soft Matter*, 2016, **12**, 5950–5958.
119 H.-F. Tseng, Y.-J. Chiu, B.-H. Wu, J.-W. Li and J.-T. Chen, *ACS Appl. Nano Mater.*, 2018, **1**, 4557–4565.
120 J.-T. Chen, P.-H. Lee, H.-F. Tseng, Y.-J. Chiu, Y.-H. Kao, K.-S. Jeng, C.-T. Liu and C.-C. Tsai, *ACS Macro Lett.*, 2015, **4**, 721–724.
121 H. Tseng, M. Cheng, K. Jeng, J. Li and J. Chen, *Macromol. Rapid Commun.*, 2016, **37**, 1825–1831.
122 L. Zheng, P. Huang, L. Zhang, D. Guo and Q. Yan, *Part. Part. Syst. Charact.*, 2016, **33**, 842–850.
123 H.-F. Tseng, M.-H. Cheng, J.-W. Li and J.-T. Chen, *Macromolecules*, 2017, **50**, 5114–5121.
124 T. Franklin, D. L. Streever and R. Yang, *Chem. Mater.*, 2022, **34**, 5960–5970.
125 J. James and R. Yang, *Org. Mater.*, 2023, **5**(2), 148–157.
126 T. Franklin and R. Yang, *Chem. Mater.*, 2023, **35**, 4955–4964.
127 K. Park, S. S. Liu, W. Tang and R. Yang, *Adv. Mater.*, 2025, **37**, 2419893.
128 P. Meakin, *Phys. Scr.*, 1992, **1992**, 31.
129 H. Lee, S. An, S. Kim, B. Jeon, M. Kim and I. S. Kim, *Sci. Rep.*, 2018, **8**, 15725.
130 J. Xu, K. Li, M. Liu, X. Gu, P. Li and Y. Fan, *Eur. Polym. J.*, 2021, **148**, 110372.
131 M. Jeyhani, S. Y. Mak, S. Sammut, H. C. Shum, D. K. Hwang and S. S. H. Tsai, *Chem. Phys. Chem.*, 2018, **19**, 2113–2118.
132 N. Doshi, A. S. Zahr, S. Bhaskar, J. Lahann and S. Mitragotri, *Proc. Natl. Acad. Sci. U. S. A.*, 2009, **106**, 21495–21499.
133 A. Dasgupta, T. Sun, R. Palomba, E. Rama, Y. Zhang, C. Power, D. Moeckel, M. Liu, A. Sarode, M. Weiler, A. Motta, C. Porte, Z. Magnuska, A. S. Elshafei, R. Barmin, A. Graham, A. McClelland, D. Rommel, E. Stickeler, F. Kiessling, R. M. Pallares, L. D. Laporte, P. Decuzzi, N. McDannold, S. Mitragotri and T. Lammers, *Proc. Natl. Acad. Sci. U. S. A.*, 2023, **120**, e2218847120.
134 J. A. Champion and S. Mitragotri, *Pharm. Res.*, 2009, **26**, 244–249.
135 H. Yang, F. Liang, Y. Chen, Q. Wang, X. Qu and Z. Yang, *NPG Asia Mater.*, 2015, **7**, e176–e176.
136 L. Tian, X. Li, P. Zhao, Z. Ali and Q. Zhang, *Macromolecules*, 2016, **49**, 9626–9636.
137 V. L. Colvin, *MRS Bull.*, 2001, **26**, 637–641.
138 H. Sun, Y. Gao, Y. Fan, J. Du, J. Jiang and C. Gao, *Macromol. Rapid Commun.*, 2023, **44**, 2300196.
139 J. E. Melzer and E. McLeod, *Microsyst. Nanoeng.*, 2021, **7**, 45.
140 T. H. Qazi, J. Wu, V. G. Muir, S. Weintraub, S. E. Gullbrand, D. Lee, D. Issadore and J. A. Burdick, *Adv. Mater.*, 2022, **34**, 2109194.

